UNIVERSITY OF OKLAHOMA

GRADUATE COLLEGE

CLOUD-RADIATIVE FEEDBACKS WITHIN THE MADDEN-JULIAN OSCILLATION

A THESIS

SUBMITTED TO THE GRADUATE FACULTY

In partial fulfillment of the requirements for the

Degree of

MASTER OF SCIENCE IN METEOROLOGY

By

Hrag Najarian
Norman, Oklahoma
2021

CLOUD-RADIATIVE FEEDBACKS WITHIN THE MADDEN-JULIAN OSCILLATION

A THESIS APPROVED FOR THE
SCHOOL OF METEOROLOGY

BY THE COMMITTEE CONSISTING OF

Dr. Naoko Sakaeda, Chair

Dr. Elinor Martin

Dr. Jason Furtado

Dr. James Ruppert

Acknowledgements

I want to first thank Dr. Naoko Sakaeda for guiding me through my master's research. I want to thank my committee members as they provided important feedbacks that led to this finished product. I cannot forget about my parents who fled war-torn Lebanon to provide their three children the best life they could. I am thankful for all the sacrifices they made for me and my brothers. As for the adversity I faced throughout my life, I thank it, I would not be who I am without it. I am grateful to have friends and colleagues who listened and supported me through the thick and the thin. I want to acknowledge someone who has had an unquantifiable impact on my life, Dr. Gail Skofronick-Jackson who we lost earlier this year. I would not be here without the funding from grant DE-SC0020188 from the Department of Energy, ASR program, thank you. I finally want to acknowledge the land I have done most of my research on (https://www.ou.edu/cas/nas/land-acknowledgement-statement). To whomever I missed, I apologize but know I acknowledge you.

Table of Contents

Abstract

The Madden-Julian Oscillation (MJO) affects weather and climate globally, however it has been challenging to accurately represent it in Global Circulation Models (GCMs) which can lead to uncertainties with future climate projections and long-term forecasts. One of the suggested processes that are important to accurately represent the MJO in GCMs is cloud-radiative feedbacks. Previous studies have suggested the MJO to be a moisture mode, where moisture is the primary factor controlling the growth and propagation of the MJO. An important contributor to moistening within this theory is the atmospheric cloud-radiative heating as it acts to sustain the MJO by moistening the tropospheric column through lifting motions that offset the added diabatic radiative energy. The MJO is also known to have stronger cloud-radiative feedbacks compared to other convectively coupled equatorial waves. The objective of this study is to use observational data from and during the DYNAMO/AMIE field campaign to investigate how cloud-radiative forcing (CRF) evolution differs between wave modes, why the MJO has a unique evolution, and how this relates to MJO dynamics under moisture mode theory.

We found that the MJO shows a structured cloud type evolution, similar to previous results where cloud types began shallow and then deepened and stratified, while the Kelvin and Westward Interio Gravity (WIG) waves saw a less structured cloud type evolution. Interestingly, most cloud types maximize in frequency after the enhanced phase of the MJO, which was not witnessed for the higher frequency wave modes. CRF evolution during the MJO was stronger and lags the enhanced phase compared to higher frequency wave modes. Our linear model which uses cloud type frequency to diagnose CRF accurately replicated CRF evolutions for all wave modes, validating the model's performance and suggesting the CRF evolution can be diagnosed by simply knowing cloud type evolution. This relationship is important for a moisture mode as this added cloud-radiative heating within wave modes translates to adiabatic lifting, which acts to moisten the tropospheric layer. Cloud-radiative moistening acts to prolong/maintain the enhanced phase of the MJO. The radiatively-driven moistening was decomposed to its contributions by different cloud types and we found that the simultaneous moistening by all cloud types is responsible for the prolonging/maintenance of the enhanced phase of the MJO. This analysis demonstrates the importance of capturing the correct evolution of different cloud

types and their radiative effects, which can be used to better understand the dynamics that govern the MJO, overall improving MJO representations in GCMs.

Chapter 1

Introduction to Wave Mode Dependence on Cloud-Radiative Effects

The Madden-Julian Oscillation (MJO), a slow (~5 m s^{-1}) eastward moving envelope of planetary scale tropical convection on an intraseasonal timescale, has challenged scientists on how to appropriately model such an oscillation since its discovery (Madden and Julian, 1971). The MJO is most convectively active through the Indian Ocean and Western Pacific, but beyond this longitudinal domain its convection becomes weaker while its circulation continues to propagate at much faster speeds (Kiladis et al., 2005). Producing accurate model representation of the MJO is important beyond just its influence on rainfall variability locally, as it has been also shown to affect rainfall variability globally (Martin & Schumacher, 2010, Alvarez et al., 2016), the Asian monsoon (Yasunari, 1979), tropical cyclone activity (Liebmann et al., 1994), ENSO events (Hendon et al., 2007), and much more (see Jiang et al., 2020 MJO review paper). Therefore, the MJO's effect on local and global weather and climate events makes the MJO a critical oscillation for numerical prediction models to depict accurately. However, global circulation models (GCMs) continue to struggle depicting the MJO, most likely due to our lack of understanding of key processes that dictate the MJO (Jiang et al., 2015).

Since its discovery, major strides in our basic understanding of the MJO have been made in theoretical, observational, and numerical modeling. Some of the current theoretical frameworks point towards cloud-radiative feedbacks, heating through the interaction between radiation and clouds, playing a key role in maintaining the amplitude (strength) and/or scale of the MJO. One of these theories, moisture mode theory, considers that water vapor is the primary factor controlling the growth and propagation of wave modes in the tropics under the assumption of a weak temperature gradient (Yu and Neelin, 1994). Weak temperature gradient (WTG) approximation stems from a weak Coriolis force which is true only over the Tropics, which ends up translating to weak geopotential (pressure) fluctuations through the momentum equation. With this assumption, the thermodynamic equation is approximately balanced with equal but opposite adiabatic and diabatic cooling/heating. Raymond (2001) related the theory of moisture mode to the MJO and argued that moisture fluctuations destabilized by cloud-radiative feedbacks are the cause for the observed MJO precipitation anomalies. For example, the presence of clouds, specifically high thin clouds, reduces radiative cooling (anomalous warming) by letting in

shortwave radiation but trapping outgoing longwave radiation (OLR), ultimately heating the tropospheric column (Harrop & Hartmann, 2016). With this added diabatic radiative heating (Q_R), there must be an equal and opposite response in vertical wind speeds that act to adiabatically cool the column, according to WTG balance. This aids in moistening the column as moist air from the lower troposphere is lofted upwards which acts to deepen convection. Overall, the moistening process ahead of the MJO, which is comprised of many processes, is the primary mode for the eastward propagation of the MJO under moisture mode theory (Maloney, 2009). With this evolution of moisture, a strong variation in cloud types (anvil, shallow, deep etc.) is also witnessed throughout its oscillation, so it becomes important to observe the evolution of cloud-radiative feedbacks, how they affect the MJO, and if existing theories are in line with observational results.

Numerous numerical modeling studies have suggested the importance of including cloud-radiative feedbacks in their studies in the existence of tropical intraseasonal variability (Benedict et al., 2020) by showing that MJO-like disturbances disappear, or its propagation speed changes when cloud-radiative effects are excluded (Lin et al., 2007, Kim et al., 2015, Bony and Emanuel, 2005). Moreover, GCMs that explicitly do not resolve clouds have a difficult time capturing the cloud-radiative feedbacks (McFarlane et al., 2007) while cloud resolving GCMs produce more accurate cloud-radiative effects and have improved representation of the MJO (Lim et al., 2018). However, cloud resolving models come at a very high computational cost and cannot realistically be applied in real-time and in climate temporal scales without limitations. Observational studies aim to continue to uncover results that can be introduced in these GCMs in forms of parameterizations to improve MJO prediction skill further without the need for computationally expensive methods.

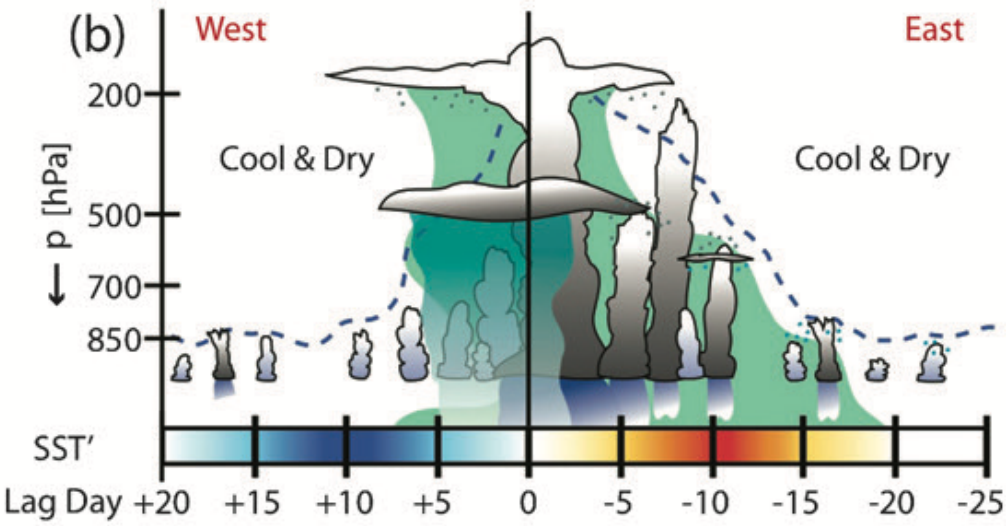

Figure 1.1: Schematic diagram of the discharge–recharge mechanism associated with the MJO. Along the horizontal axis appears SST' [red (blue) indicates warmest (coolest) anomalies] and the lag days relative to the day of maximum rainfall (day 0). Stages of the discharge–recharge process, as seen in ERA-40 data, are listed below the lag days. The approximate top level of convective cloud processes is indicated by the dashed blue line, while green shading represents the general area of q'>0. Light blue dots above shallower convective clouds represent moistening via detrainment, while gray dots below stratiform cloud types represent ice crystal fallout and moistening. Convective precipitation is indicated by darker blue rain shafts, and stratiform precipitation is light blue and slightly transparent. (figure & caption credit: Benedict & Randall, 2007).

Different cloud types have inherent properties that allow for unique interactions with radiation. Coupled with a strong variation in cloud types and moisture throughout the MJO lifetime, its cloud-radiative feedback also evolves and becomes a complicated and crucial factor to consider (Riley and Mapes et al., 2011, Feng and McFarlane et al., 2014, Ciesielski et al., 2017). Figure 1.1 shows the cloud and moisture evolution of the MJO at a fixed location over the Indian Ocean. Clouds begin shallow during the suppressed phase (negative lag days in Fig. 1), but as the moist layer deepens through a variety of processes such as large-scale horizontal moisture transport (Zhu and Hendon, 2015) and vertical moisture advection from the clouds themselves, clouds can grow deeper and convection can grow upscale (Benedict and Randall, 2007). During the enhanced phase of the MJO when precipitation rate is maximized (zero lag days in Fig. 1), organized convective systems such as meso-scale convective systems (MCSs) dominate the local region, spreading large swaths of anvil and cirrus clouds (Powell and Houze, 2013). The transition from shallow and scattered convection to more organized forms of convection alter cloud type fractions (i.e., stratiform cloud types) when transitioning to the

enhanced phase of the MJO (Riley and Mapes et al., 2011). These upper-level clouds take up a large area and have the tendency to reflect incoming solar shortwave (SW) radiation (secondary importance), while trapping outgoing terrestrial longwave (LW) radiation (primary importance), ultimately resulting in less radiative cooling to occur (anomalous warming) throughout the tropospheric column (Ciesielski et al., 2017). After the enhanced phase has passed and the vertical moisture profile becomes top heavy, high precipitating and non-precipitating cloud types continue to persist (Riley and Mapes et al., 2011).

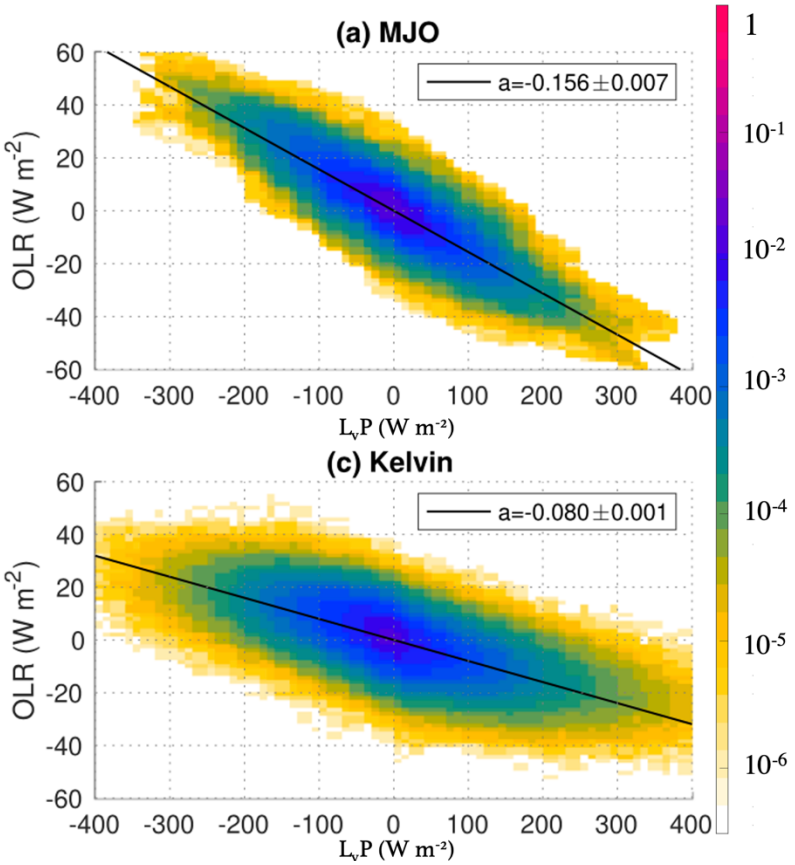

Figure 1.2: Shading shows the distribution of wave-filtered TMPA 3B42 rainfall (P) and OLR anomalies for 0.02 mm hr^{-1} and 2 W m^{-1} bins. The rainfall on the horizontal axis is multiplied with the latent heat of vaporization (L_v). Black line shows the regression coefficients of OLR onto rainfall, which represents the cloud-radiative feedback parameter. The regression coefficients and its 95% confidence interval are shown in the legend of each panel (figure & caption credit: Sakaeda et al., 2020).

Previous studies have used the slope between precipitation rate and OLR to quantify the strength of cloud-radiative feedback, which will be referred to as "cloud-radiative feedback parameter". An example of such slope for the MJO and Kelvin waves is shown in Fig. 1.2. As

convective clouds intensify into deep convection and/or organize into MCSs, both precipitation rate and vertical moisture transport increase. The production of high stratiform cloud types from increased deep and organized convection traps OLR (decrease in OLR). The stronger this relationship, the more efficient the equatorial wave mode is in supporting high cloud types that trap OLR, supplying stronger anomalous radiative warming that can act to maintain or amplify the wave. Recent studies have found that this relationship depends on wave number frequency of convective disturbances (Adames and Kim, 2016, Inoue et al., 2020, Sakaeda et al., 2020). These studies found that higher frequency and wavenumber wave modes (i.e., convectively coupled Kelvin and Westward Inertial Gravity waves) have weaker cloud-radiative feedback parameter compared to a wave mode with a lower-frequency and wavenumber such as the MJO (Fig. 1.2). Adames and Kim (2016) suggested that the enhanced horizontal spreading of anvil type clouds for longer wavelength waves could be responsible for the increase in their measured cloud-radiative feedback parameter when related to wavenumber. Lin and Mapes (2004) also suggested that high sheared environments within a deep tropospheric layer (150-700hPa) produced higher cloud total fractions, higher cloud tops, and lower OLR. Building on the finding that the strength of cloud-radiative feedbacks varies between wavenumbers, Inoue et al. (2020) and Sakaeda et al. (2020) both showed that the MJO has the strongest cloud-radiative feedback parameter compared to other wave modes. Under the assumption of WTG, vertical velocity profile is closely related to diabatic heating. Therefore, a wave mode with a top-heavier vertical velocity profile produces more upper-level clouds, leading to increased trapping of OLR when compared to a bottom-heavy profile where more mid-level clouds exist under this regime (Inoue et al., 2020). While the MJO produced the most top-heavy vertical velocities compared to other wave modes, Sakaeda et al. (2020) did not find a clear one-to-one relationship between the strength of cloud-radiative feedback and top heaviness of vertical velocities among all the waves. This unclear relationship between vertical velocity profiles and cloud-radiative feedback parameter emphasizes the need to understand the cause(s) of why exactly cloud-radiative feedback parameter strengthens with decreasing frequency and wavenumber and if upper-level clouds are the primary reason why the MJO has the strongest cloud-radiative feedback parameter.

While some studies have examined the cloud-radiation interaction within the MJO (Genio and Chen 2015, Ciesielski et al. 2017), there has not been a study that answers why the MJO has a uniquely strong cloud-radiative evolution than other wave modes. This gap in knowledge is

problematic as the aforementioned moisture mode theory relies on cloud-radiative interactions as a part of its core framework. Therefore, further investigating the MJO cloud-radiative interactions from observations is a critical step to properly apply the important cloud-radiation interaction in numerical model simulations. This aids in assigning a theoretical framework to the MJO, leading to a concrete understanding of the MJO itself that can be used to improve mid-to-long-term forecasting as well as GCMs.

By utilizing data during the Dynamics of the MJO/Atmospheric Radiation Measurement (ARM) MJO Investigation Experiment (DYNAMO/AMIE) field campaign, we will answer two questions: 1) How does the evolution of cloud-radiative forcing depend on wave mode and 2) What mechanism(s) drives the MJO to have a unique cloud-radiative forcing evolution. DYNAMO/AMIE was conducted over a region that is largely free from any major topographical features, resulting in data collection over open-ocean-like environments, important in isolating the dynamics that drive the MJO to answer the listed questions above.

Chapter 2

The Evolution of Cloud-Radiative Forcing and Cloud Types Between Wave Modes

In this chapter we will discuss the data sets and methods that set the groundwork for this research. We then will analyze cloud type and moisture evolution within varying wave modes. Cloud-radiative forcing measurements are then analyzed for each wave mode, giving us insight on which cloud type(s) could be responsible for the strong and unique cloud-radiative forcing evolution that only the MJO experiences.

2.1 Data utilized during DYNAMO/AMIE

We utilize data sets that were collected during the Dynamics of the MJO/Atmospheric Radiation Measurement (ARM) MJO Investigation Experiment (DYNAMO/AMIE) field campaign. This field campaign aimed to address two main problems: low MJO simulation skill, especially during the initiation phase over the Indian Ocean, and the low subseasonal-to-seasonal and climate forecasting skill from state-of-the-art global models. During this field campaign, well-coordinated instrumentation across the Indian Ocean was able to capture three MJO signals. The intensive observation period of the field campaign which provides higher resolution data from 1 October 2011 to 9 February 2012 will be utilized. The observational instruments used in this study were deployed over an atoll over the Indian Ocean, which provide a close to open ocean environment during this analysis.

National Center for Atmospheric Research (NCAR) dual-wavelength Doppler polarimetric S-band and Ka-band (S-Polka) radar was deployed at Addu City, Maldives on Gan Island (0.63S, 73.10E) during the intensive observational period of the field campaign. Utilizing Steiner et al. (1995) algorithm updated by Powell et al. (2016), S-PolKa radar retrievals categorized precipitating clouds into convective, stratiform, mixed (mix of convective and stratiform), shallow, isolated, and weak precipitating types. This radar-derived product provides 15-minute 1-km horizontal gridded precipitating cloud type retrievals over a 150-km radius, providing us with a time series of rain rate evolution over the DYNAMO/AMIE intensive observation period. A notable limitation within this product is the inability to accurately detect rain rates during suppressed conditions, specifically after January (Powell and Houze, 2013). More in-depth information on the radar derived products is provided in Powell et al. (2016).

The Pacific Northwest National Laboratory (PNNL) Combined Remote Sensor retrieval algorithm (CombRet) is utilized in this study to provide a vertically resolved and integrated view of shortwave and longwave radiative heating profiles in both clear and all-sky conditions. Cloud-radiative forcing (CRF) is then calculated by taking the difference between the all and clear-sky radiative heating rates, providing us information on the cloud-radiative impacts. This data set combines retrievals from the Active Remote Sensing of Clouds (ARSCL) product using Ka-band ARM Zenith Radars (KAZR) as well as S-PolKa retrievals located on Gan Island (Feng et al., 2014). The S-Polka and KAZR reflectivity's were merged to capture both deep convection and non-precipitating high-clouds. This algorithm also provides microphysical retrievals (temperature and moisture) and computed radiative fluxes and heating rate profiles at a 90 m vertical resolution every 30-seconds from 10 October to 31 December, 2011. These retrievals have a high temporal and vertical resolution at a singular point over Gan Island, providing a local vertically resolved view of CRF and microphysical evolution.

The Clouds and Earth's Radiant Energy System (CERES) Edition 3A provides a global 1-by-1 degree gridded 3-hourly averaged integrated top-of-atmosphere (TOA) and surface radiative fluxes under clear and all-sky conditions between the dates of 1 March 2000 to present day (Wielicki et al., 1996). CRF is calculated using CERES data, providing an averaged view of CRF compared to CombRets singular point view of CRF. This study specifically focuses on atmospheric CRF that is calculated through the CRF at TOA and surface. A 3-by-3-degree grid box centered over Gan Island is used to average atmospheric CRF at each 3-hourly time step. The time-average and diurnal cycle during 10 October 2011 to 31 December 2011 was removed for both CERES and CombRet data to create comparable anomalous atmospheric CRF over Gan Island without the diurnal influence.

2.2 CombRet Cloud Type Classification

CombRet data also provides estimated heights of cloud base and top, which can be used to examine a distribution of cloud layer frequency over Gan Island. Figure 2.1 shows this cloud type frequency by cloud base and top heights. Following Riley and Mapes (2009) classification of cloud types, 6 cloud types were classified: (A) cumulus humilis (shallow), (B) cumulus congestus (congestus), (C) cumulonimbus (deep), (D) altostratus and altocumulus (mid), (E) detached anvil (anvil), and (F) cirrus (cirrus). Shallow, congestus, and deep clouds are classified

as precipitating cloud types while mid, anvil, and cirrus cloud are classified as non-precipitating cloud types. These cloud types are separated by 2 levels in both cloud top (at 4.5 km and 10 km) and cloud base (3 km and 7 km) heights. Riley and Mapes (2009) classified these cloud types by using the natural delineations of cloud type frequencies that were measured through a satellite-based radar (CloudSat) which also appears in the CombRet data (Fig. 2.1). A caveat to be aware of when using this method of classifying cloud types is that the deep and congestus cloud types are not exclusively convective because precipitating stratiform clouds are lumped in this category as well. This is because CombRet detects precipitation reaching the ground as a low cloud base, ~0 km, meaning precipitating anvil and mid clouds are categorized into deep and congestus cloud types respectively. Alongside CombRets and CERES CRF measurements, this cloud type data allows the comparison of atmospheric CRF and the observed cloud types detected overhead. This provides a direct observation of cloud type's impact on the vertical and integrated structure of radiative heating in the atmosphere between varying wave modes.

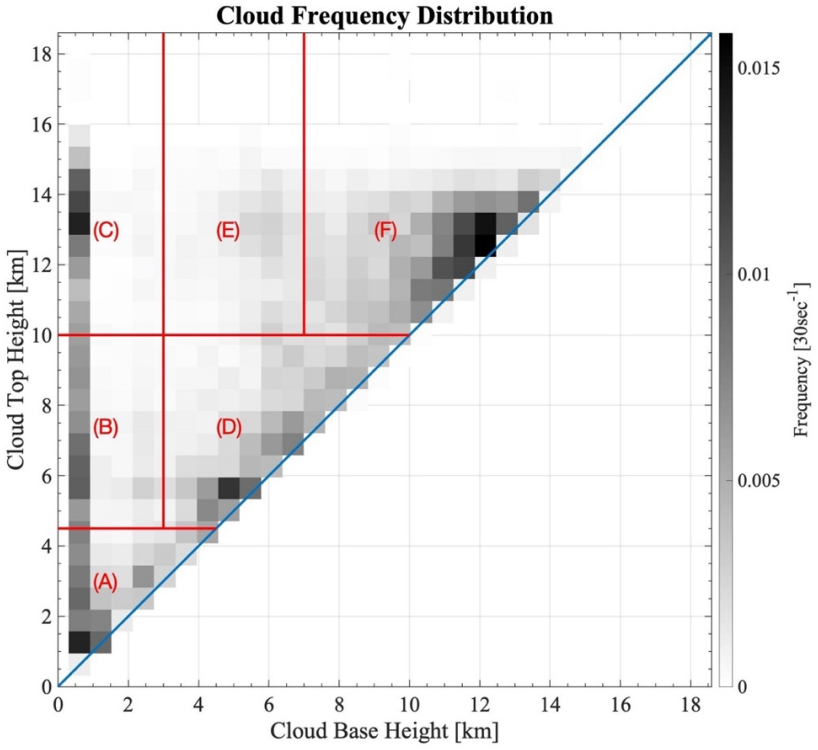

Figure 2.1: Binned CombRet estimated cloud base and top height frequency [30 sec^{-1}] retrievals from Oct 10-Dec 31 are plotted as a function of frequency in black and white bins. Solid blue line indicates the separation of impossible from possible measurements, meaning cloud base < cloud top always. Vertical red lines are natural delineations that separate classified cloud types: (A) Cumulus Humilis (Shallow), (B) Cumulus Congestus (Congestus), (C) Cumulonimbus (Deep), (D) Altostratus and Altocumulus (Mid), (E) Detached Anvil (Anvil), (F) Cirrus (Cirrus).

2.3 Wave Mode Identification

The aforementioned datasets provide variables that are critical in understanding how cloud type and CRF evolve, however, a method is required to compare these variables between varying wave modes. There are various ways of defining the phase of a wave mode, but because the measurements in this study are mainly over a specific region over the Indian Ocean, defining phases of wave modes through locally based indices provides a more accurate representation instead of using well-known EOF (Empirical Orthogonal Function) based indices such as RMM (Real-time Multivariate MJO) index (Wheeler & Hendon, 2004). EOF-based indices identify the amplitude and state of the MJO based on the projections of global patterns, which do not necessarily identify the local state of the MJO accurately. We use the Tropical Rainfall Measurement Mission (TRMM) version 3B42 v7a rain rates to define a local index of each wave mode. This data set provides 3-hourly precipitation rates at 0.25-by-0.25-degree resolution globally between 50°S–50°N from 1998–2019, however spatial resolution is regridded to 2.5-by-2.5-degree resolution for this study (Huffman et al., 2007). Firstly, three wave modes will be analyzed in this study: the MJO (zonal wavenumber 0 to 10, periods 20 to 100 days), the Kelvin wave (zonal wavenumber 1 to 15, periods 2.5 to 17 days, equivalent depth 8 to 90 m), and the Westward inertia gravity (WIG) wave (zonal wavenumber −15 to −1, periods 1.25 to 3.33 days, equivalent depth 8 to 90 m). TRMM rainfall anomalies are filtered for these waves by performing the inverse of Fourier transform coefficients of specified wavenumber and frequency, following the method of Wheeler and Kiladis (1999). A 7.5-by-7.5 degree area centered over Gan Island is located and precipitation rates are spatially averaged. Following Riley et al. (2011) method, we then standardize the wave-filtered precipitation rate anomaly and its time tendency using their climatological standard deviations from 15ºS–15ºN over the whole equatorial belt. We specifically chose the Kelvin and WIG wave modes to compare with the MJO because our region of study resides near the equator (0.63S, 73.10E), where other wave modes with off-equatorial centered convection will not be well-captured (Wheeler and Kiladis, 1999).

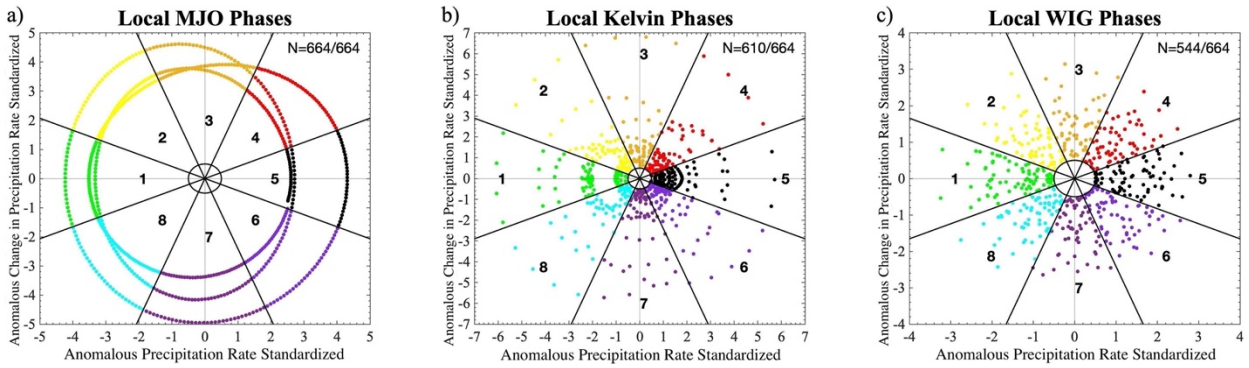

Figure 2.2: Locally based indices derived through TRMM 3-hourly standardized (15ºS–15ºN) precipitation data shows a pinwheel-like plot of precipitation and change in precipitation for the MJO (a), Kelvin wave (b), and WIG wave (c). Each color/wedge represents a phase of the wave modes, with 1 and 5 being the suppressed and enhanced phases respectfully. The inner solid circle represents standard deviation threshold set (> 0.5 std). N value at the top right indicates # of 3-hourly timesteps that passed said threshold.

By plotting these two variables against each other, a "pinwheel" for each wave mode is constructed (Fig. 2.2). We can split the wheel into 8 phases and this results to phase 1 representing the suppressed phase, phases 2-4 represent the suppressed-to-enhanced transition, phase 5 represents the enhanced phase, and phases 6-8 represents the enhanced-to-suppressed transition. Lastly, to remove weak wave mode signals, an amplitude threshold is set (> 0.5 std) for each time-step to pass. The amplitude is defined as the combined precipitation rate and change in precipitation rate, which is simply the distance from the point on the pinwheel to the center. This threshold results in all 664 MJO 3-hourly time steps retained, 610 Kelvin wave time steps retained, and 544 WIG wave time steps retained. The amount of time steps retained is important to note as it will create differences in spreads when applying significance tests. Roughly, 3 MJO, 11 Kelvin wave, and 38 WIG wave events occurred between 10 October and December 31, 2011. The obvious limitation here is the limited wave mode data we have over this time period. While statistical significance testing suggests some of our results are significant to the 95th percentile, having a short temporal resolution is a limitation since an argument can be made that these events are outliers. We plan to expand the datasets we use well outside of the temporal bound in future work to provide more statistically stable results. Otherwise, these locally based indices allow for an intercomparison between varying wave modes unlike EOF based indices since interpreting effects locally between wave modes would be near impossible using EOF based indices. The MJO shows strong signals that easily pass the threshold while

higher frequency wave modes have time-steps that do not pass the threshold, which are excluded from the analysis.

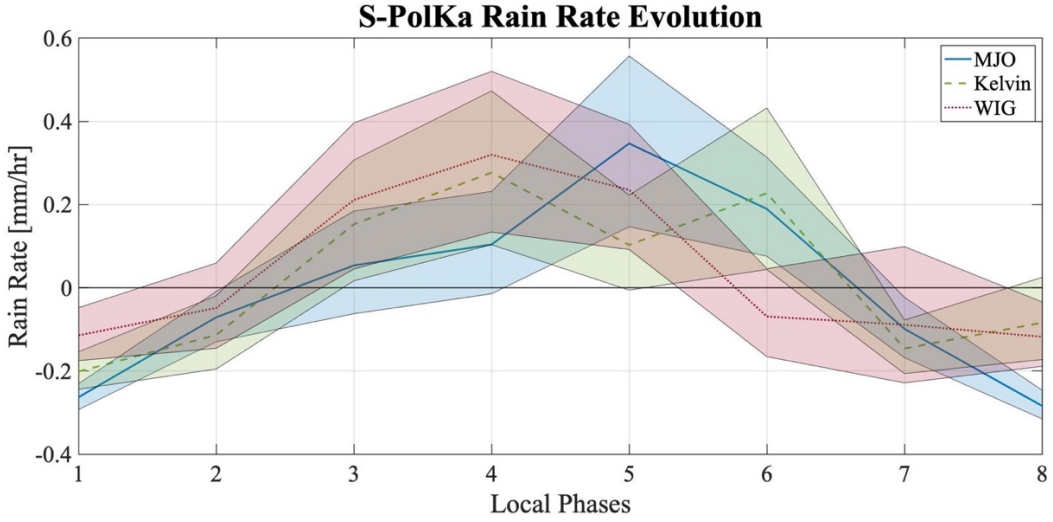

Figure 2.3: S-PolKa radar derived anomalous domain averaged rain rate [mm/hr] evolution during Oct-10 to Dec-31 are composited over 8 local phases for each wave mode (-Blue: MJO, --Green: Kelvin, ···Red: WIG). Shading represents 95% significance. Phases 1/5 represents the suppressed/enhanced phase respectfully.

S-PolKa rain rates are composited using the local wave phase for all wave modes and 95% significance test is conducted to examine the evolution of ground-based radar estimates of rain rate (Fig. 2.3). Significance is determined through 10,000-iterations of bootstrapping dates within each phase number with repetition and recalculating cloud type frequencies for each phase. 95% significance was found by sorting the 10,000 values for each phase number and taking the 2.5 and 97.5 percentile values as the lowest and highest bounds respectfully. This type of significance test will be used throughout this study unless specified otherwise. Figure 2.3 shows that the estimated local rain rates from S-PolKa evolve differently for each wave mode. Recall that the locally defined wave indices follow rain rates to minimize at phase 1 and maximize at phase 5. The MJO follows this definition while the Kelvin wave experiences a double peak of rain rate at phase 4 and phase 6, and the WIG wave peaks at phase 4. S-Polka has much smaller domain area (~70,500km^2) compared to TRMM (~692,500km^2), which is a plausible cause for differences in rain rates and phase between the two data sets, hence why S-PolKa domain averaged rain rate evolution does not follow TRMM's for the higher frequency wave modes. These deviations may exist between the two instruments due to a variety of reasons (i.e. instrumentations, estimation algorithm, resolution, filter/unfiltered, etc.); however, S-PolKa

detects maximum rain rates to occur around the enhanced phase, providing another reliable rain rate measurement to utilize. Significance testing shows the error bars for each wave mode and how consecutive phases have overlapping error bars, suggesting that the wave-specific evolutions are not significantly different at the 95th percent threshold.

2.4 The Evolution of Cloud Types

With these methods, we first explore how cloud types evolve within each wave mode. 30-second cloud type frequency measurements from CombRet are averaged into 3-hourly time steps to match the temporal frequency of the local phases of wave modes. Bins that correspond to each cloud type are summed to get 3-hourly cloud type frequency for all 6 cloud types. Utilizing the locally defined phases, we composite the 6 varying cloud type frequencies to determine the average evolution of each cloud type frequency within each wave with a significance test done through bootstrapping (Fig. 2.4). For the MJO (blue), congestus and deep cloud types maximize during the enhanced phase of the MJO when rain rate maximizes (phase 5), while mid, anvil and cirrus cloud types lag the enhanced phase, maximizing during the transition from enhanced to suppressed (phase 6 and 7). While shading (error bars) for each wave mode overlap frequently between phases, the evolution of cloud types is consistent with previous studies that looked at MJO cloud type evolution over a much longer period of time (Riley & Mapes, 2011). Generally, all cloud types exhibit similar evolutions between wave modes, however, while not significant, the MJO produces more frequent deep and anvil cloud types during their respective peaks in frequency.

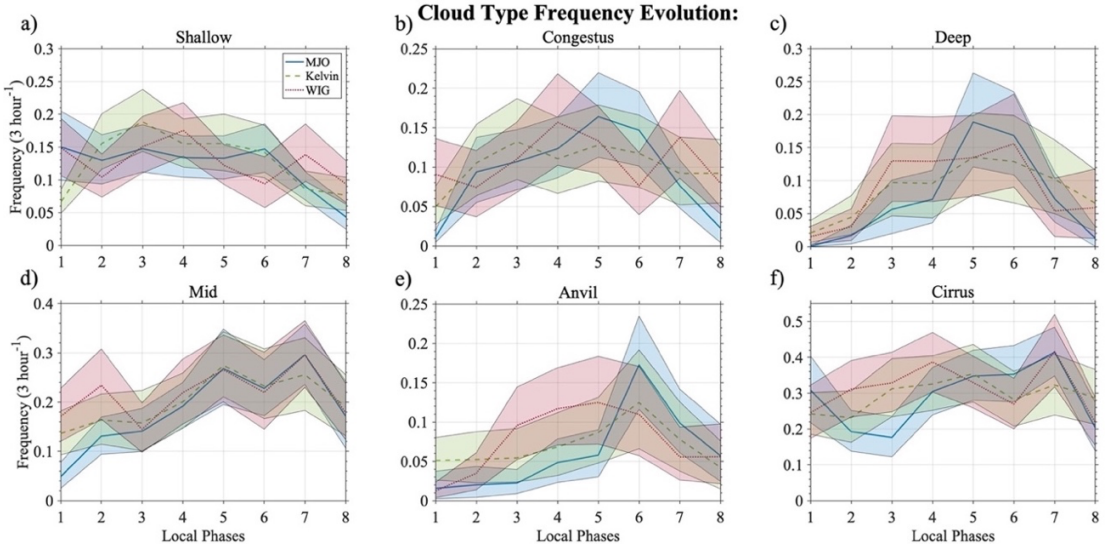

Figure 2.4: CombRet derived cloud type frequencies [3 hour^{-1}] composited over 8 local phases for each wave mode (-Blue: MJO, --Green: Kelvin, ···Red: WIG). Shading represents 95% significance. Top row (a, b, c) represents precipitating convective cloud type evolution, and the bottom row (d, e, f) represents non-precipitating stratiform like cloud type evolution.

To visualize where each cloud type maximizes for each wave mode, we examine the evolution of cloud frequencies defined by cloud height and top bins shown in Fig. 2.1 with wave phase and identify the wave phase at which the cloud frequency maximizes. This analysis shows what specific combination of cloud base and top heights maximize at which phase of a wave mode (left column, Fig. 2.5). Notice that the non-precipitating stratiform cloud types (mid, anvil, and cirrus) maximize at phases 6, 7, and 8, as shown in Fig. 2.4. The right column of Fig. 2.5 shows the range (maximum minus minimum) of cloud frequency in each cloud type bin, where higher values indicate large fluctuation of cloud type frequencies during the lifecycle of the wave mode. 95% significance is tested for each bin by comparing the observed cloud frequency range between the 8 phases for each wave mode with a range that is calculated by randomizing and repeating cloud frequency at each phase using all timesteps from each wave mode. Since randomized range will be much smaller than the observed, if the observed range is larger than the top 95th percentile randomized range, it is considered significant indicated by a stipple. This figure provides an objective overview on what phase cloud types are most frequent for each wave mode without the need to set arbitrary bounds on cloud base and top heights. The MJO experiences predominant shallow clouds during the suppressed phase and congestus and some deep clouds during the transition towards the enhanced phase. The enhanced phase is comprised

of frequent deep, congestus and mid clouds while anvil and cirrus clouds are most frequent during the transition from enhanced to suppressed. Cloud frequency range indicates that the fluctuations in the evolution for all cloud types are significant for the MJO. However, the latter cannot be said for the higher frequency wave modes. While cloud types show high range in frequency for higher frequency wave modes (Kelvin and WIG), these waves do not exhibit a clear and organized pattern of cloud type evolution that is witnessed with the MJO. This result suggests that the MJO influences cloud type evolution within the larger scale envelope of convection, while this influence is weaker for the Kelvin and WIG waves. More specifically, both deep and anvil clouds simultaneously maximize at phases 5, 6, and parts of 7 for the MJO but this is not exhibited by the Kelvin and WIG waves. More research is needed to understand why this difference in cloud type evolution exists between the MJO and higher frequency wave modes, and if the cloud type evolution influences the MJO and not the other way around.

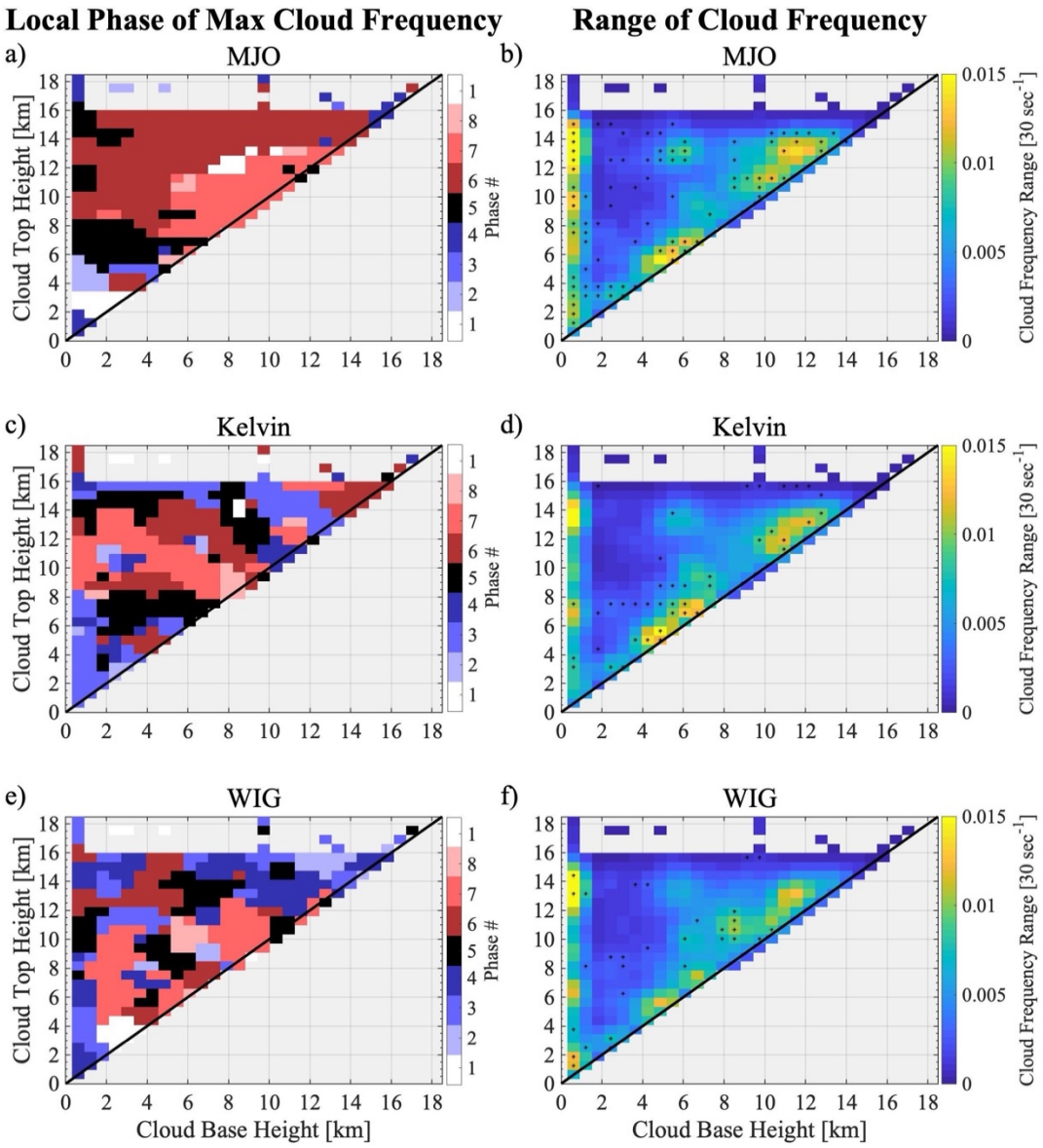

Figure 2.5: Left column (subplot a, c, e) represents bins of cloud base and top height that maximize at local phases for each wave mode. Frequency distributions were smoothed by a center weighted mean in both x and y-axes. Note that this is an objective view of what Fig. 2.4 shows. Right column (subplot b, d, f) represents the range (maximum - minimum) of frequencies [30 sec^{-1}] at each bin. Stippling represents 95% significance.

2.5 The Evolution of Atmospheric Cloud-Radiative Forcing

Since cloud type evolution differs between wave modes, we should expect CRF to also differ. After compositing vertically integrated CRF from both CombRet and CERES, we can now compare CRF evolution between wave modes (Fig. 2.6). Both datasets show a similar

evolution, where the MJO exhibits the largest CRF values compared to the higher frequency waves modes. Both CERES and CombRet data show that the MJOs maximum value in CRF is higher than both the Kelvin and WIG waves. While significant error bars overlap for both data sets and all wave modes, the MJOs CRF evolution follows CombRet CRF evolution in Ciesielski et al. (2017) study, adding to our confidence that the MJOs evolution is correct and has a larger atmospheric CRF maximum compared to higher frequency wave modes. A larger atmospheric CRF amplitude suggests that the MJO is associated with a greater absorption or trapping of longwave radiation from clouds and/or a weaker cloud albedo which increases the chance of shortwave radiation absorption within the atmosphere. In the previous section we noted that some cloud type frequencies have larger amplitudes for the MJO compared to the higher frequency wave modes. More frequent occurrences of cloud types lead to greater cloud-radiative effects, potentially leading to the larger CRF amplitudes that we see for the MJO in Fig. 2.6.

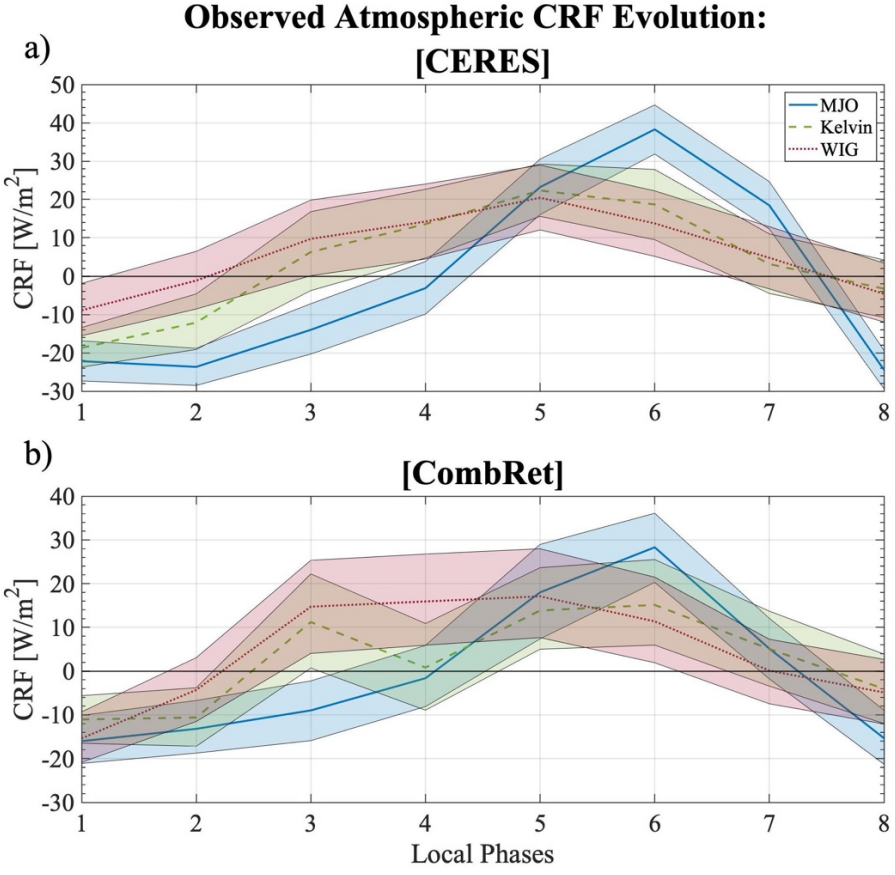

Figure 2.6: Evolution of integrated anomalous atmospheric cloud-radiative forcing [W/m^2] over 8 phases of varying wave modes (-Blue: MJO, --Green: Kelvin, ···Red: WIG). Shading represents 95% significance. Subplot a) utilizes anomalies from the CERES data set while subplot b) utilizes the CombRet data set.

There also exists a lagged relationship of CRF from maximum precipitation rates that only occurs within the MJO, meaning CRF maximizes AFTER precipitation rates maximize. Significance test of CERES data shows this lagged relationship is significant, with CombRet data depicting a similar lagged evolution, both of which is not witnessed with either the Kelvin or WIG waves. This unique lagged relationship indicates that the MJO cloud type evolution is influencing the atmospheric CRF to lag compared to higher frequency wave modes. Previous studies have found the MJO to exhibit a similar lagged CRF relationship (Ciesielski et al., 2017) while others have documented a leading relationship (Genio & Chen, 2015) where CRF maximizes before precipitation rates maximize. We hypothesize these opposing results may stem from differences in the data utilized. Studies that depict a leading relationship of CRF within the MJO utilized sun-synchronized twice-daily polar orbiting satellite data (CloudSat). A caveat in utilizing these data sets is its inability to document the full, uninterrupted cloud type evolution within a wave mode, allowing for an unintentional diurnal CRF bias to exist within the analysis itself. Studies that have witnessed a lagged relationship utilized continuous data streams which inherently include the diurnal evolution of CRF, avoiding the diurnal bias present in twice-daily satellite data. However, it is important to note that CombRet's short data collection period and singular point retrievals are a caveat since long-term satellite data produce more statistically stable results from their larger dataset. The difference in span of data collected could suggest that the three MJO signals during the DYNAMO/AMIE period were outliers in terms of the lagged CRF relationship. Since the datasets utilized in this study are continuous, it can capture the diurnal evolution of CRF alongside the evolution on cloud types, which cannot be captured through satellite based CRF measurements. Therefore, at least within DYNAMO/AMIE period and domain, we hypothesize this unique lagged relationship of high-cloud type frequency and CRF are related.

Prior studies that investigated the cloud-radiative feedback parameter found the MJO to have a higher parameter compared to higher frequency wave modes shown in Fig 1.2 (Adames and Kim, 2016, Inoue et al., 2020, Sakaeda et al., 2020). To confirm prior findings, we utilize rain rates from S-PolKa and plot the relationship between atmospheric CRF and rain rate anomalies for each wave mode (Fig. 2.7). While this analysis is different from previous studies that calculated cloud-radiative feedback parameter as the relationship between OLR and rain rate, utilizing atmospheric CRF instead of OLR provides a more direct relationship between

atmospheric warming and precipitation. Figure 2.7a utilizes domain averaged S-PolKa rain rates and CERES CRF values while Fig. 2.7b utilizes single point CombRet rain rates and CRF values. Therefore, Fig. 2.7a represents an averaged cloud-radiative feedback relationship, while Fig. 2.7b represents a localized relationship where influence from isolated storms over Gan Island can occur, resulting in the inability to characterize the larger scale cloud-radiative feedback relationship well. For this reason, we will focus on Fig. 2.7a, where the MJO has a higher cloud-radiative feedback parameter, decreasing in parameter as wavenumber increases to Kelvin and WIG waves. Notice that the 95% significance tested slopes (m values in legend) overlap, however error bars do show a decreasing trend as wavenumber increases. Higher frequency wave modes indicate a smaller/weaker slope between rain rate and atmospheric CRF compared to the MJO, increasing in value as wavenumber decreases. This is in line with previous studies that also suggested a similar relationship with rain rate and OLR anomalies. As mentioned in Chapter 1, previous studies suggested that the enhanced horizontal spreading of anvil type clouds occur at greater frequencies for equatorial waves of longer wavelengths. However, here we suggest that the reason for the larger cloud-radiative feedback parameter for the MJO is due to the lagged CRF relationship. Precipitation rate decreases after the enhanced phase, but CRF still continues to increase. This leads to values with low precipitation rates and high CRF values, ultimately leading to a steeper slope. We suggest that the lagged CRF is driven by a compounding effect from various cloud type effects on atmospheric CRF. The left column of Fig. 2.5 showed that a great majority of cloud types maximize at phase 6 for the MJO compared to higher frequency wave modes, resulting in a compounding effect on atmospheric CRF. While we are not disproving previous hypotheses on the wavenumber-cloud-radiative feedback parameter relationship, we argue that the deep and high cloud types maximizing simultaneously at phase 6 are important to increasing the cloud-radiative feedback parameter.

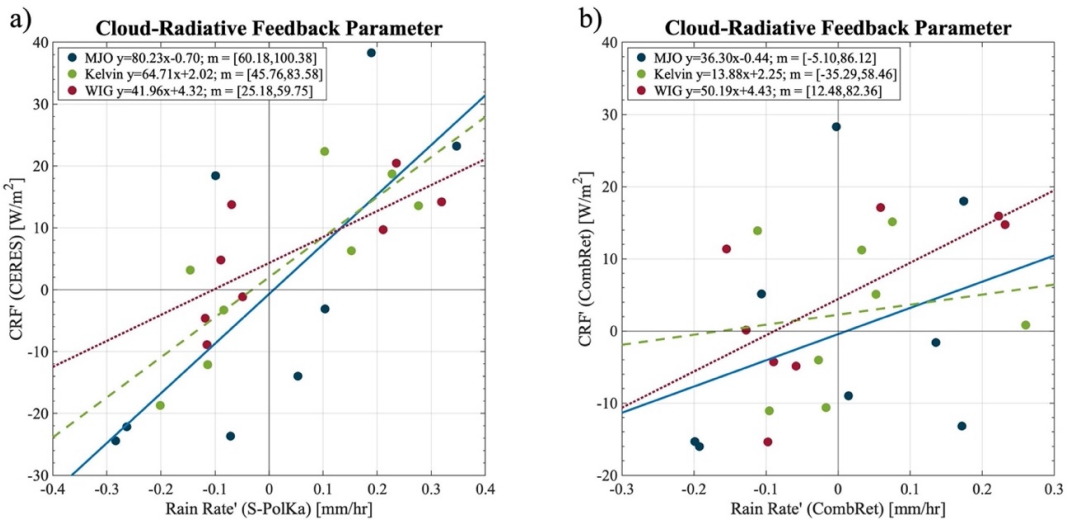

Figure 2.7: Composited S-PolKa rain rates anomalies [mm/hr] and CERES atmospheric CRF anomalies [W/m^2] from each wave mode and phase are plotted against each other a) while CombRet rain rates and atmospheric CRF anomalies are plotted on b). A linear regression line is fit for all wave modes (-Blue: MJO, --Green: Kelvin, ···Red: WIG). The slope of this line represents the cloud-radiative feedback parameter. Legend labels each wave modes linear equation ($y = mx + b$) where y is the diagnosed CRF anomaly, m is the slope/cloud-radiative feedback parameter, x is the rain rate anomaly, and b is the y-intercept. 95% significance test is shown by the thresholds of slope m in the legend.

We also utilize vertically resolved radiative retrievals from CombRet to composite the evolution of CRF between varying wave modes to get a better sense of the vertical structure of CRF evolution (Fig. 2.8). Areas with stipples indicates areas of significant anomalous heating or cooling. The MJO (Fig. 2.8a-c) experiences a lagged relationship of CRF to enhanced precipitation throughout the entire tropospheric column, matching the evolution of column-integrated CRF from CERES and CombRet from Fig. 2.6. The longwave anomalous warming during phase 5 (enhanced phase) and 6 (enhanced-to-suppressed transition) in the mid-to-low levels and shortwave anomalous warming during phase 5 and 6 in the upper-levels from the MJO are consistent with previous studies that looked at CombRet data during DYNAMO (Ciesielski et al. 2017). Both longwave and shortwave CRF warming increase in the vertical from phase 5 to 6, leading to maximum warming throughout the troposphere at phase 6. There is also a substantial upper-level cooling effect that occurs in the longwave during phase 5 due to high cloud tops which emit at much cooler temperatures, leading to a negative total CRF response. To our knowledge, what has not been previously observed are the evolution of vertical CRF profiles for the Kelvin (Fig. 2.8, d-f) and WIG (Fig. 2.8, g-i) waves, which show some deviation from the

MJO's evolution. The Kelvin wave experiences increased heating rates early on during phase 3, and then again at phase 5 and 6. This bimodal peak in CRF is witnessed in the CombRet integrated atmospheric CRF plot (Fig. 2.6 b) but was not witnessed with the CERES CRF dataset. The WIG wave experiences a somewhat similar total CRF evolution as the MJO, however measurements are shifted towards earlier phases than the MJO. These unique evolutions of observed CRF within varying wave modes are inherently affected by cloud types and their evolution. The next chapter will analyze this cloud type and CRF relationship to understand what is causing the unique evolutions of CRF that is witnessed within wave modes.

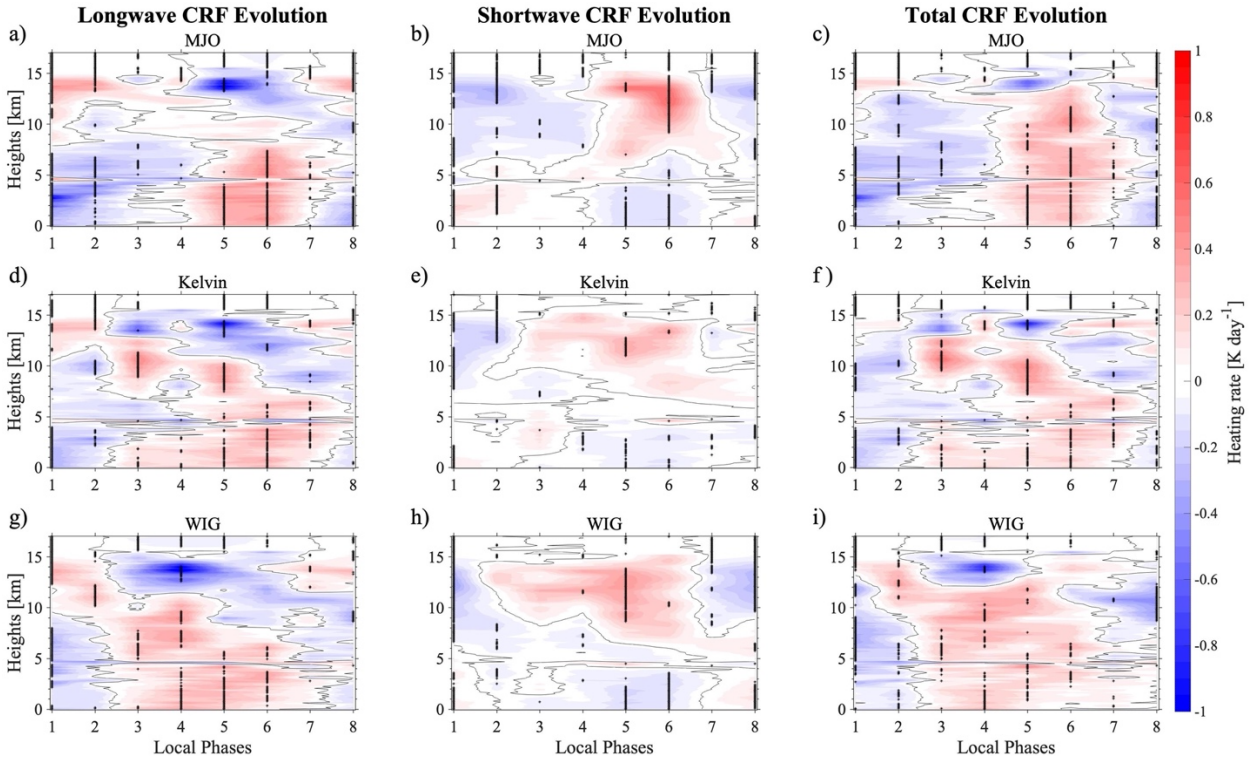

Figure 2.8: CombRet vertically resolved CRF anomalies [Kday^{-1}] in the longwave (left column), shortwave (middle column), and total $LW + SW$, right column) are composited for each wave mode (MJO, a-c; Kelvin wave, d-f; WIG; g-i). Black stippling represents areas of positive/negative significance to the 95%. Solid black line represents the zero line.

Chapter 3

Quantifying Contribution to CRF by Cloud Type

The previous chapter suggested that the cloud type evolution of the MJO could be influencing the unique CRF evolution. To test this hypothesis, we devise a simple linear regression model to capture the relationship between cloud type frequency and CRF. This model will be compared to observed results to check the model's ability to construct CRF and more importantly, analyze individual cloud type contribution to CRF to determine which cloud type(s) is responsible for the unique CRF evolution of the MJO.

3.1 Linear Model Specifications

A linear regression model is devised to decompose the contribution of atmospheric CRF evolution by each cloud type at Gan-Island during 10 October to 31 December 31 2011. CombRet provides net atmospheric CRF which provides CRF values from all existing cloud types since multiple cloud types can exist during a 3-hour timestep. Our analysis will attempt to diagnose how each cloud type contributes to the net atmospheric CRF. 3-hourly cloud type frequencies and integrated 3-hourly total atmospheric CRF anomalies from both CERES and CombRet (after averaging 30-sec retrievals into 3-hourly bins) will be utilized in our simple linear model. A linear regression is applied between cloud type frequency and net atmospheric CRF measurements for all 6 cloud types individually, where cloud type frequency is the independent variable (x) and CRF is the dependent variable (y). This equation is an example of the analysis,

$$\widehat{Q'}_{dp}(t) = mF_{dp}(t) + Q_o \quad Eq.1$$

where $\widehat{Q'}_{dp}(t)$ is the column-integrated anomalous atmospheric CRF contributed from deep clouds at each time step, m is the slope representing heating rate frequency per deep cloud type frequency, $F_{DP}(t)$ is the deep cloud type frequency at each time step, and Q_o is the CRF when deep cloud type frequency is zero. This equation is applied to all 6 cloud types where $\widehat{Q'}_{sh}$, $\widehat{Q'}_{cg}$, $\widehat{Q'}_{md}$, $\widehat{Q'}_{av}$, $\widehat{Q'}_{ci}$ represent anomalous atmospheric CRF associated with shallow, congestus, mid-level, anvil, and cirrus clouds, respectively. This allows us to find a linear relationship between net atmospheric CRF and the cloud type frequency overhead during that measurement. This

means that all scatter points in Fig. 3.1a-f all have the same atmospheric CRF values (y-axis) but differing cloud type frequency.

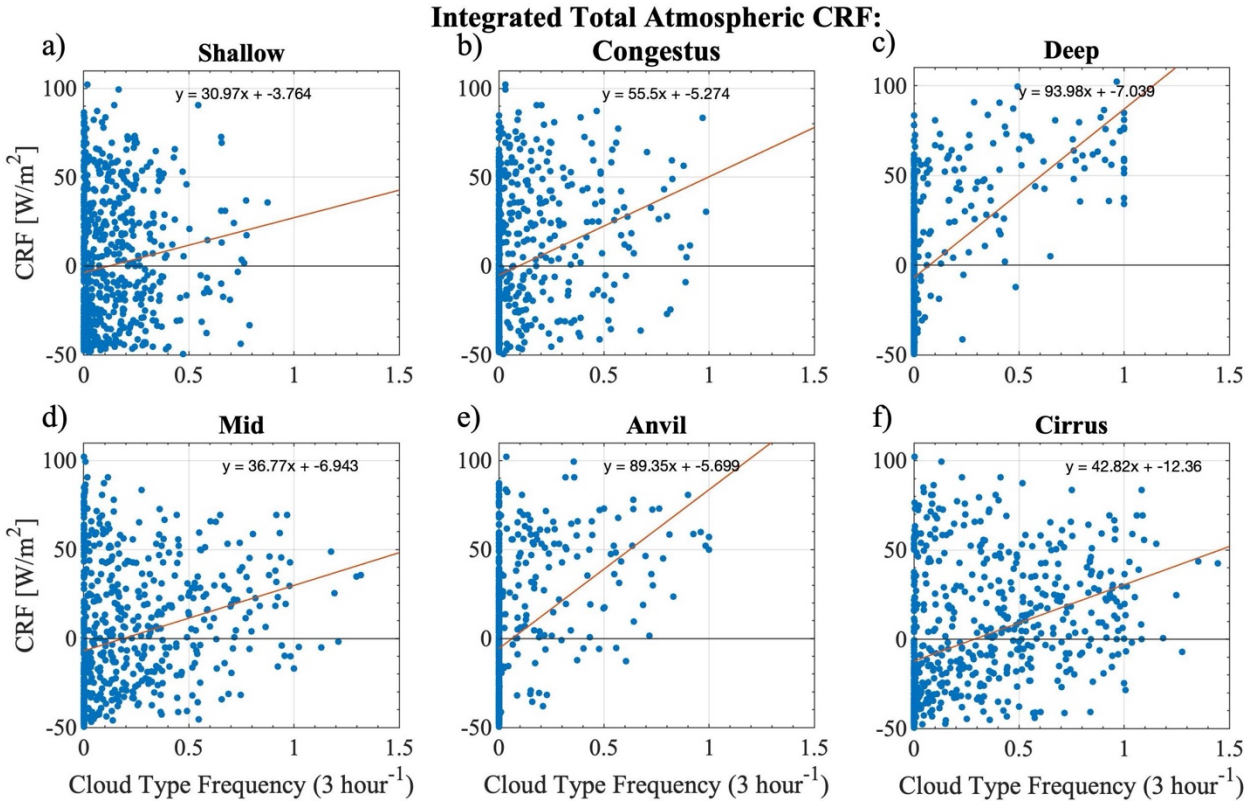

Figure 3.1: Scatter plot of CERES total ($LW + SW$) atmospheric CRF anomalies [W/m^2] with the respective cloud type frequency [3 hour^{-1}]. The red line is the best fit line with the equation $y = mx + b$, where m is the slope, b is the y-intercept, y is the total atmospheric CRF anomaly, x is the cloud type frequency, that best describes the linear relationship at the middle-top of the inner subplot.

Figure 3.1 shows the scatter plot of each cloud type frequency's relationship to CRF with a best fit line. This analysis was executed using both CERES and CombRet (not shown) integrated total atmospheric CRF measurements. Both models agreed that deep and anvil cloud types are the most influential in increasing CRF (large slope/m). We suspect this because these two cloud type trap more longwave terrestrial radiation than any other cloud type. While the shortwave component does interact with these cloud types and does contribute to warming, most of the warming from shortwave interactions is confined in the upper-atmosphere, and the cooling effect is weak in the lower atmosphere. Note that deep and anvil cloud types are related to one another since deep convection produces anvil clouds, meaning anvil clouds are dependent on deep clouds. However, this relationship is checked by applying a lag correlation test on cloud type

frequency evolution after a deep cloud type detection (not shown). The analysis showed anvil cloud types are significantly more frequent 3 hours before and after deep cloud type detection, backing the claim that anvil cloud types exist during times of deep convection, suggesting that CRF measurements of deep and anvil cloud types will somewhat be related. While these two specific cloud types are somewhat related, the lag correlation analysis did not show similar significant relationships existing with other cloud types during times of congestus and shallow cloud type detection, suggesting CRF measurements associated with other cloud types are more independent. Note that these relationships cannot all be perfectly linear ($R^2 = 1$) since if one cloud type frequency is a perfect linear match with CRF, then the other five cloud types would explain 0% of the variations, showing a poor linear fit ($R^2 = 0$). Therefore, it is by design that the linear relationships between individual cloud type frequencies and CRF are not perfectly linear. Also note that there are non-zero values of atmospheric CRF when some cloud frequencies are zero. While at that 3-hour timestep the cloud frequency of a cloud type is zero, other cloud frequencies can be greater than zero during that timestep which can lead to non-zero values of atmospheric CRF. To test which cloud types most contribute to CRF and how well these cloud types collectively predict CRF the 6 individual cloud type regression equations in Fig. 3.1 are summed together to get the "all" cloud type contribution to CRF (i.e., $\hat{Q}'_{all} = \hat{Q}'_{sh} + \hat{Q}'_{cg} + \hat{Q}'_{dp} + \hat{Q}'_{md} + \hat{Q}'_{av} + \hat{Q}'_{ci}$). This method of summing the regressed equations ensures that each cloud type's unique CRF relationship is retained, rather than a method where a single regression is done over the sum of all 6 cloud type frequencies, which would simply capture the average CRF response from a cloud, regardless of the type.

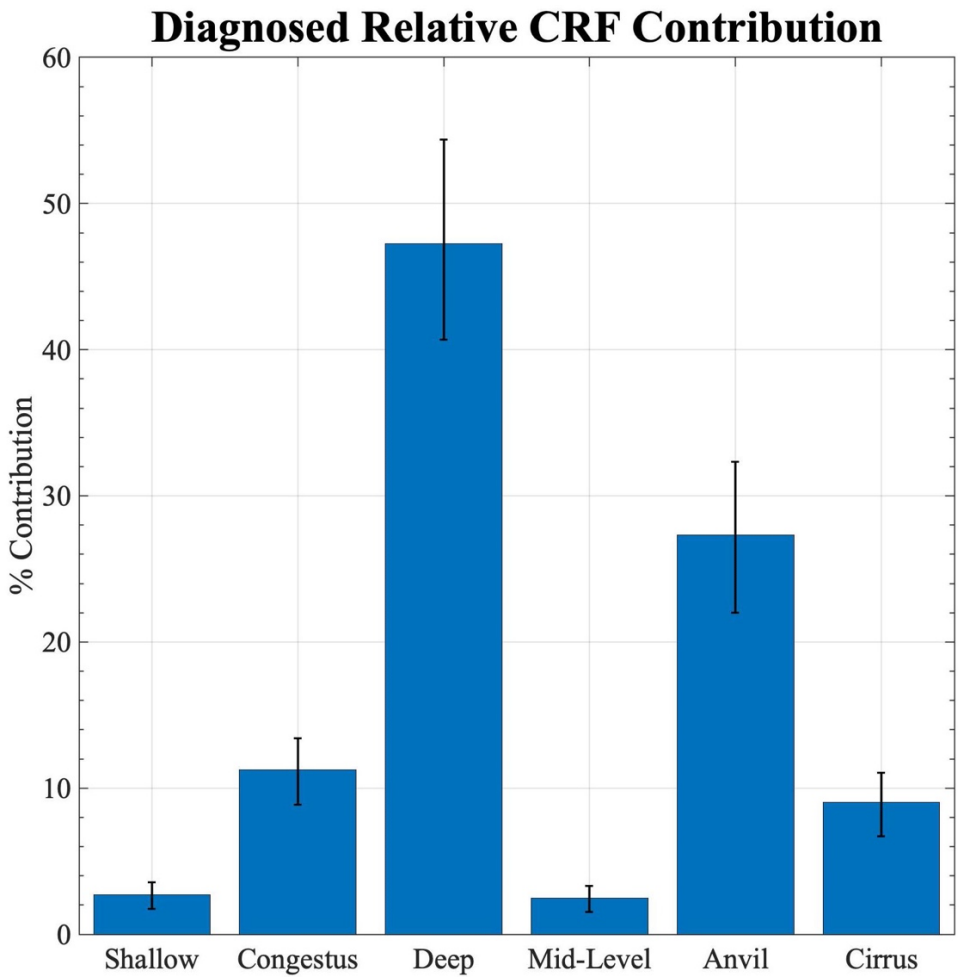

Figure 3.2: Diagnosed relative anomalous total ($LW + SW$) integrated atmospheric CRF contribution by cloud type compared to all cloud type contribution. Local CombRet CRF measurements are used to diagnose the model, and error bars represent variation of contribution per cloud type when applied 95% significance test.

This allows the ability to isolate each cloud type's relative contribution to integrated atmospheric CRF (Fig. 3.2). Percentage contribution refers to the ratio of CRF contribution from a cloud type compared to all cloud type contribution. Error bars represent 95% significance through bootstrapping, where overlapping error bars represents cloud type contribution that are not significantly different from one another. CombRet CRF data is used in this case since relating localized cloud type measurements to local CRF measurements is a direct comparison rather than using CERES CRF measurements that are averaged over a 3-by-3-degree area which would include CRF influences from various other cloud types that are not being detected by CombRet. These results validate the suggestion that deep and anvil cloud types are the most influential cloud types since they contribute the majority of all diagnosed CRF. While the

deconstructed cloud type relationships with integrated CRF appears weakly correlated (Fig. 3.1), when you combine the 6 cloud type contributions to CRF (all cloud type contribution), the relationship between observed and diagnosed CombRet measured CRF shows a close 1-to-1 relationship (Fig. 3.3). This indicates a strong correlation with an R^2 value of 0.78 using CERES and 0.68 using CombRet (not shown) observed and diagnosed CRF.

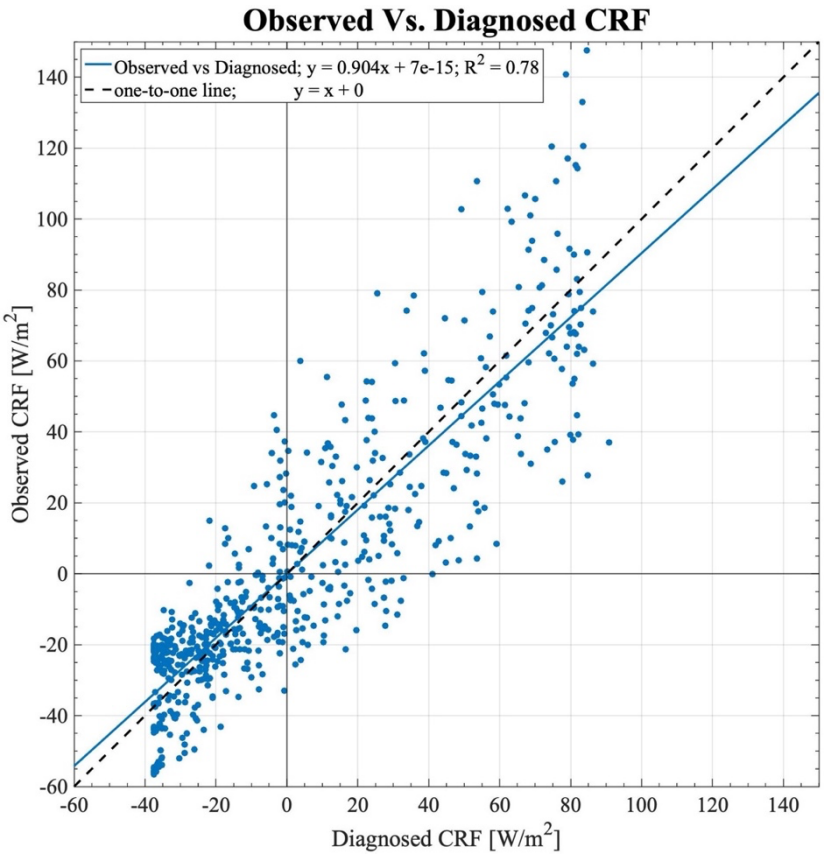

Figure 3.3: Scatter of observed CERES total ($LW + SW$) component of integrated atmospheric CRF anomalies [W/m²] and its diagnosed value via linear model based on cloud type frequency. Linear regression line is plotted in solid blue, and a one-to-one relationship is shown for comparison in black dashed. Legend includes linear equation in form of $y = mx + b$, and R^2 value indicating strength of correlation.

Furthermore, we can utilize the vertically resolved anomalous total CRF measurements from CombRet and apply the same method we used with the integrated CRF measurements. A set of linear regression for each cloud type, like in Fig. 3.1, is applied at each vertical layer, where the slope, or heating rate frequency, at each vertical layer is plotted on the horizontal axis (Fig. 3.4). Shading represents 95% significance through bootstrapping which depict areas of significant heating/cooling when shading does not overlap the vertical solid zero line. This figure provides

insight on the effect individual cloud types have on CRF vertical profile. The 6 cloud type vertical heating rate frequency profiles are unique, suggesting that each cloud type induces independent CRF effect. Notably, precipitating convective cloud types (Fig. 3.4 a-c) show significant positive heating rate frequencies below and/or within the cloud, with deep cloud types significantly heating the atmosphere below 10 km. Nonprecipitating stratiform cloud types (Fig. 3.4 d-f) act somewhat differently. Mid clouds tend to show weak but significant heating below 4 km, while anvil clouds show significant and strong heating below 10 km, with maximum heating occurring between 6-8 km as well as significant cooling occurring between 12-16 km. Cirrus cloud types show weak but significant heating between 7-13 km. Generally, the longwave component is the dominating factor when it comes to cloud-radiative heating, however the shortwave CRF component does play a role in warming the mid-to-upper levels.

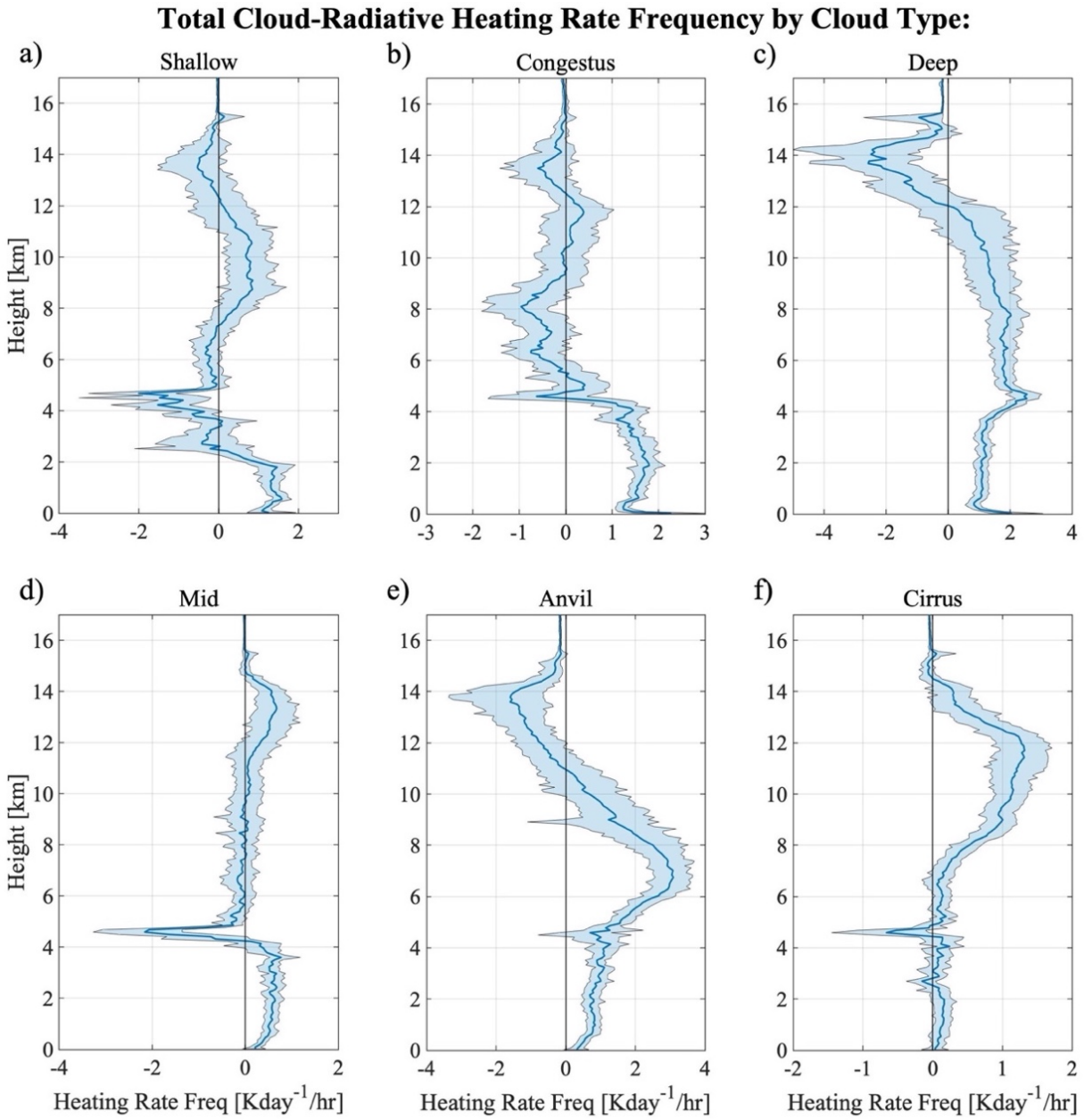

Figure 3.4: CombRet vertically resolved anomalous total ($LW + SW$) CRF values are linearly regressed against the respective cloud type frequencies. The slope (m) of the linear regression at each vertical height is plotted indicating heating rate frequency in $Kday^{-1}$/hour. Shading represents 95% significance, where significant positive/negative heating occurs when shading does not overlap the vertical solid x=0 line.

If we sum together the six-cloud type contributions to cloud-radiative heating, we can diagnose the net CRF influence from all cloud types during the DYNAMO field campaign (Fig. 3.5). As mentioned before, the longwave component (Fig. 3.5a) is the dominate feature here (i.e.,

from the context of the mass-weighted column integral), however, the shortwave component (Fig. 3.5b) contributes positive CRF heating at the 7-15 km heights. This leads to total CRF heating between 11-13 km where it would not be the case if it was not for the shortwave component (Fig. 3.5c). While significance tests do not show substantial significant CRF heating/cooling at any height interval, the raw values do suggest that cloud-radiative interactions act to heat much of the troposphere (0-13 km) as total heating is positive below the 13 km height. Given these results, we move to apply this diagnostic linear model with observed cloud types to test how well it captures CRF evolution within varying wave modes.

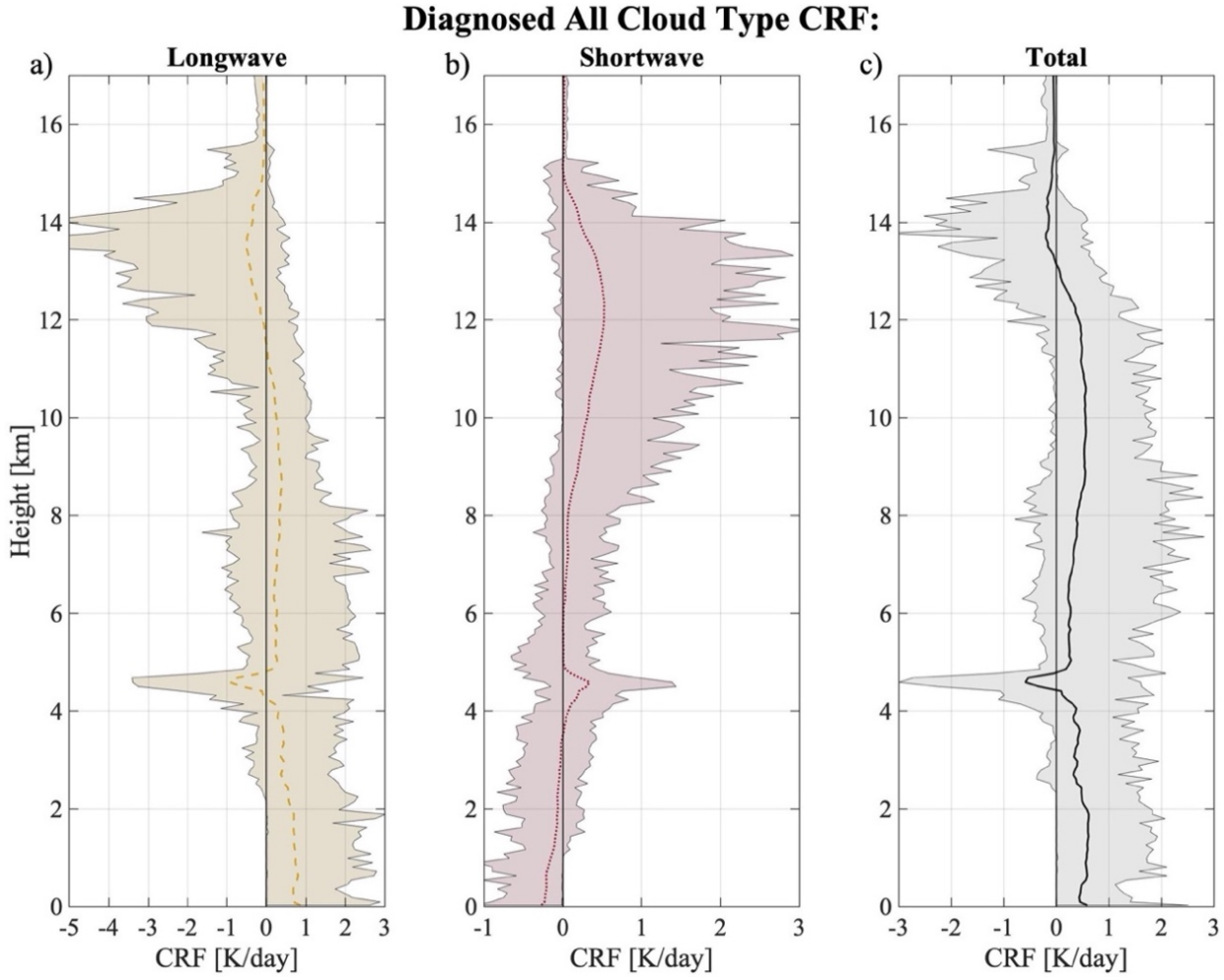

Figure 3.5: CombRet vertically resolved anomalous longwave (a), shortwave (b), total ($LW + SW$, c) CRF values are linearly regressed against 'all' cloud types. All cloud type contribution to CRF is calculated by a sum of the 6 individual cloud type regressions. The diagnosed CRF anomaly (y) of the linear regression at each vertical height is plotted indicating heating rate by CRF in K/day. Shading represents 95% significance, where significant positive/negative heating occurs when shading does not overlap the vertical solid x=0 line.

3.2 Diagnosing CRF Evolution

These sets of linear equations ($y = mx + b$) can be leveraged to diagnose the integrated atmospheric CRF values (y) by inputting the respective cloud type frequencies at each 3-hourly timestep (x). The diagnosing of CRF is confined to just the DYNAMO period as this model's purpose is to diagnose the cloud type-CRF relationship rather than to be used as a predictive model. To get all cloud type contribution, the CRF is diagnosed for the six cloud types using the linear regression models and then is summed together and composited for each wave mode (Fig. 3.6). This analysis is done with the linear model based on CERES (Fig. 3.6 a) and CombRet (Fig. 3.6 b) anomalous column-integrated total atmospheric CRF values, where significance test follows the method used in Fig. 2.6. The diagnosed atmospheric CRF evolution for the MJO maximizes at phase 6 for both CERES and CombRet CRF initiated models, after the enhanced phase has passed, consistent with observational results shown in Fig. 2.6. The MJO also continues to show a higher CRF maximum compared to the Kelvin and WIG wave modes, also consistent with observational results. While phase 6 is not the significant maximum for the MJO, these diagnostic results share similarities with observed results, suggesting that the MJOs lagged CRF relationship with precipitation can be diagnosed by simply knowing the cloud type overhead.

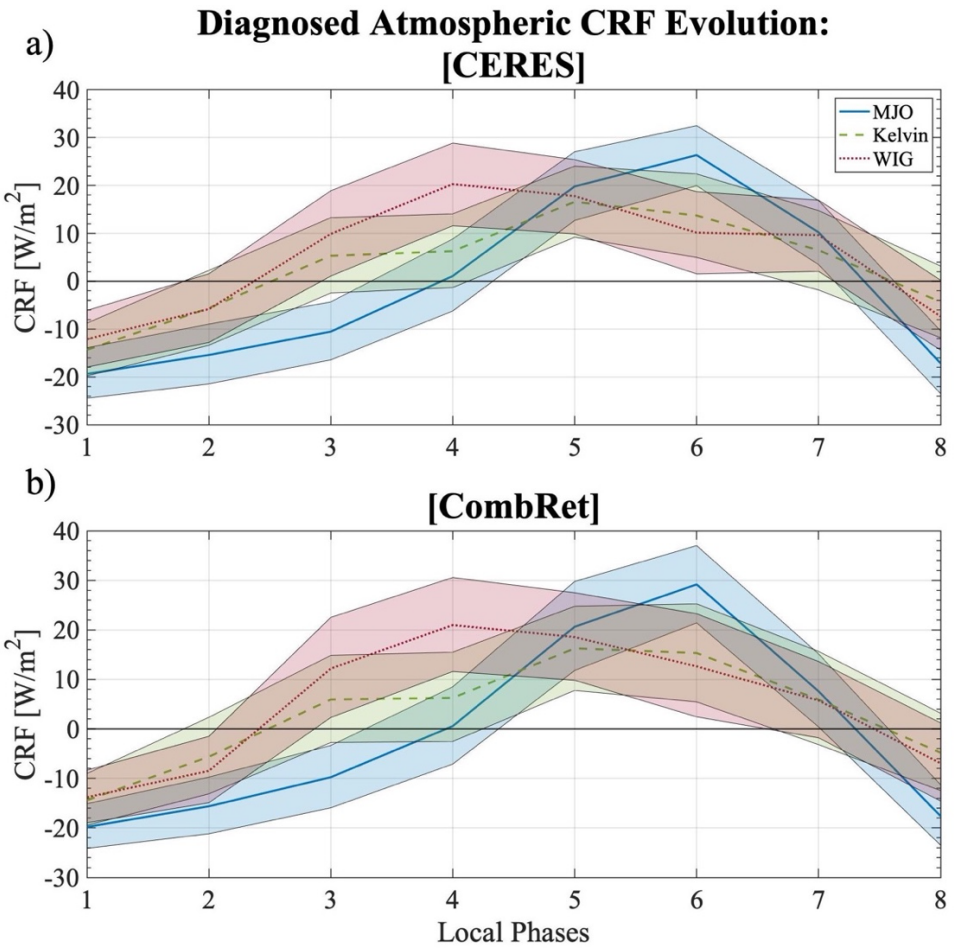

Figure 3.6: Same as Fig. 2.6 but diagnosed with a set of linear equation.

We can utilize the sets of linear equations from CombRet's vertically resolved CRF data set to diagnose how the vertically resolved anomalous CRF evolves with varying wave modes given only cloud type frequencies (Fig. 3.7). The reconstructed CRF through linear regression models for MJO (Fig. 3.7 a-c) shows a very close comparison of CRF evolution in longwave, shortwave, and total columns compared to the observed. One small exception is that the longwave CRF cooling maximum around 15 km was diagnosed to be at phase 6, while observations indicate it minimizes during phase 5. Otherwise, the linear model reconstructed the MJOs total CRF maximum at phase 6 and overall evolution quite well. The higher frequency wave modes generally depict the observed CRF evolution well, however they are not captured as well as the MJO. This is either due to the less data points higher frequency wave modes had to work with because of weak wave mode signals not passing the threshold set as seen in Fig. 2.2b-c, or it could be that higher frequency wave modes simply do not have as high of a CRF variation as the

MJO (Fig. 3.7 d-i). The model does not capture the observed mid-to-upper-level longwave warming the Kelvin wave experienced during phase 3 and 5 and the observed upper-level longwave cooling at phase 4 of the WIG wave seems to have stretched from phase 3-to-6 in the diagnosed evolution. These exceptions occur near the height that all cloud shortwave and longwave heating rate frequencies are of equal but opposite magnitudes, leading to cancelations and insignificant heating/cooling at those heights (not shown). However, even given the shortcomings, the linear model captures the general vertically resolved CRF evolution well enough. The performance in diagnosing both integrated and vertically resolved CRF emphasizes the importance of cloud types to accurately diagnose CRF evolution within these wave modes. Being able to diagnose CRF evolution is important since this added diabatic heating into the system leads to moistening through vertical motions through adiabatic lifting under WTG approximation, as described next. This moistening process is fundamental within the moisture mode framework which is often used to describe the dynamics of the MJO.

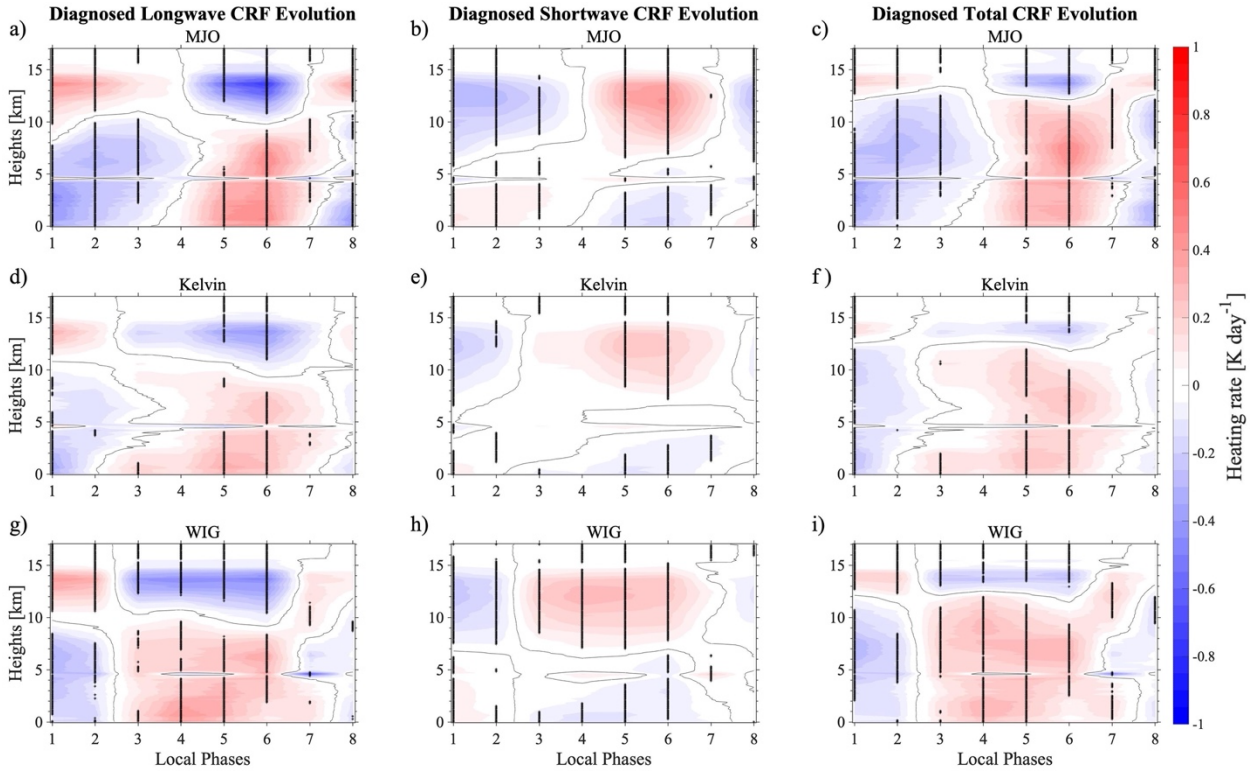

Figure 3.7: Same as Fig. 2.8 but diagnosed with a set of linear equation.

Chapter 4

Quantifying the Cloud-Radiative Contribution to Moistening

This study so far has investigated the cloud-radiative interactions of the MJO, Kelvin, and WIG waves. These interactions are of importance as they are a source of added diabatic heating. Under the WTG approximation, this added diabatic heating is brought to equilibrium through vertical motions to cool, in turn resulting in moistening the atmosphere within wave modes. The magnitude and evolution of this moistening that is driven by cloud-radiative process has implications on the fundamental characteristics such as propagation speed and intensity of wave modes. This chapter will investigate the contribution of moistening through cloud-radiative effects within the MJO, attempting to better understand the potential affects it would have on wave mode characteristics. We only examine the MJO in this section since the WTG assumption we invoke, which enables a direct link between heating and moistening, is less applicable to the higher frequency wave modes.

4.1 Assumptions and Conceptualization

The MJO is often described as a moisture mode, where fundamental dynamics are determined by the processes that control the moisture field. Weak temperature gradient (WTG) approximation is necessary in this framework. This approximation utilizes the inherent weak Coriolis force over the tropics, translating into weak geopotential (pressure) fluctuations within the momentum equation, suggesting weak temperature gradients can be applied over tropical regions. When applied to the thermodynamic equation, diabatic heating/cooling is balanced by adiabatic cooling/heating respectively. Consider how the dry static energy (s) budget would change when this approximation is applied,

$$\frac{\partial s}{\partial t} + \vec{v}_h \cdot \nabla s + \omega \frac{\partial s}{\partial p} = Q_1 \quad Eq.2$$

$$s = c_p T + gz$$

where c_p is the specific heat capacity of dry air ($c_p = 1004\ (\frac{J}{kgK})$), T is temperature, g is gravitational acceleration, and z is geopotential height. Without WTG applied, the time tendency of s is dependent on the horizontal and vertical advection of s and Q_1, which is the apparent heating (Yanai et al., 1973). Under the WTG approximation, the above equation simplifies to,

$$\omega \frac{\partial s}{\partial p} = Q_1 = Q_R + Q_C \quad Eq. 3$$

where Q_R represents the radiative heating component and Q_C is the latent heating from condensation and vertical heat flux associated with the convective process. Assuming $\frac{\partial s}{\partial p}$ does not change, vertical velocity (ω) is only influenced by two processes: radiative heating and latent heating. Therefore, ω can be split into ω_R and ω_C, where each ω corresponds to the vertical velocity contributed by their respective diabatic heat sources which act to balance adiabatic cooling:

$$\omega = \omega_C + \omega_R \quad Eq. 4$$

$$\omega_R = Q_R \left(\frac{1}{\partial s/\partial p}\right) \quad Eq. 5$$

$$\omega_C = Q_C \left(\frac{1}{\partial s/\partial p}\right) \quad Eq. 6$$

This breakdown allows us to quantify contributions of radiatively-driven moistening ($-\omega_R \frac{\partial q}{\partial p}$) in the column-integrated anomalous specific humidity tendency equation (Eq. 7).

$$\langle \frac{\partial q'}{\partial t} \rangle = -\langle \vec{v}_h \cdot \nabla q \rangle' - \langle (\omega_C + \omega_R) \frac{\partial q}{\partial p} \rangle' + (E - P)' \quad Eq. 7$$

$$\langle A \rangle = \frac{1}{g} \int_{P_T}^{P_S} A \, dp$$

$$\langle -\omega_R \frac{\partial q}{\partial p} \rangle' = \langle -Q_R \left(\frac{\partial q/\partial p}{\partial s/\partial p}\right) \rangle' \quad Eq. 8$$

Brackets indicate vertical integration between P_S of 1000 hPa and P_T of 200 hPa and primes indicate anomalies from time-mean during DYNAMO period. From the left-hand side to the right-hand side of Eq. 7; $\langle \partial q'/\partial t \rangle$ represents the vertically integrated local moisture tendency, $\langle \vec{v}_h \cdot \nabla q \rangle'$ represents the vertically integrated horizontal advection of moisture, $\langle (\omega_C + \omega_R)\, \partial q/\partial p \rangle'$ represents the vertically integrated vertical advection of moisture through convective and radiative processes, and $E - P$ represents moisture source through evaporation (E) minus moisture sink through precipitation (P). We will focus on $\langle (\omega_R) \partial q/\partial p \rangle'$ calculated as Eq. 8 and how it contributes to $\langle \partial q/\partial t \rangle$.

We note that the WTG approximation is not a valid approximation for all wave modes in the tropics. Wolding et al. (2016) suggests that the MJO is governed by different dynamics than

convectively coupled equatorial waves. Their study found that where the WTG approximation is most relevant is limited to wave modes with planetary eastward-propagating wavenumber and intraseasonal timescales that applies to the MJO, therefore WTG approximation is not applicable for WIG waves and for high frequency Kelvin waves. Since the MJO is the only wave mode that fits the WTG approximation in this study, this chapter will focus solely on how moisture tendency evolves within the MJO.

4.2 Moisture Evolution

First, ω_R is calculated from Eq. 5 using CombRet 30-second vertically resolved microphysical measurements of temperature and specific humidity and anomalous total ($LW + SW$) CRF as Q_R, averaged into 3-hourly to match the temporal resolution of local wave phase. To calculate ω_R, Q_R is divided by $\partial s/\partial p$, but there are some values of $\partial s/\partial p$ extremely close to zero which, when divided by said small value, results in extremely large ω_R value that are physically unrealistic. To remove these outliers, the bottom and top .1% of ω_R values are removed, allowing for the removal of extremely strong negative and positive vertical wind speeds but also retaining 99.8% of the data. Once calculated, ω_R and the vertical gradient of specific humidity ($\partial q/\partial p$) is substituted into Eq. 8, resulting in a 3-hourly time-series of vertically integrated radiatively-driven moisture tendency. A 2-day running average is applied onto the vertically integrated results to better capture the general evolution. This 2-day running is a short enough time where it has little to no effect on an intraseasonal wave mode like the MJO. These values are then composited to their respective local phases of the MJO, and 95% significance is calculated through bootstrapping for each phase.

Figure 4.1 shows the vertically integrated radiatively-driven moisture tendency evolution in solid blue, $\langle -\omega_R \partial q/\partial p \rangle'$, and the dashed red line represents the vertically integrated anomalous moisture evolution $\langle q \rangle'$. The moisture evolution of the MJO significantly maximizes during the enhanced phase while radiatively-driven moisture tendency continues to increase after the enhanced phase, with a significant maximum at phase 6 and a continuation of positive moisture tendency into phase 7. This suggests that the radiatively-driven moistening continues to moisten after peak total moisture which occurs at phase 5, during the enhanced phase.

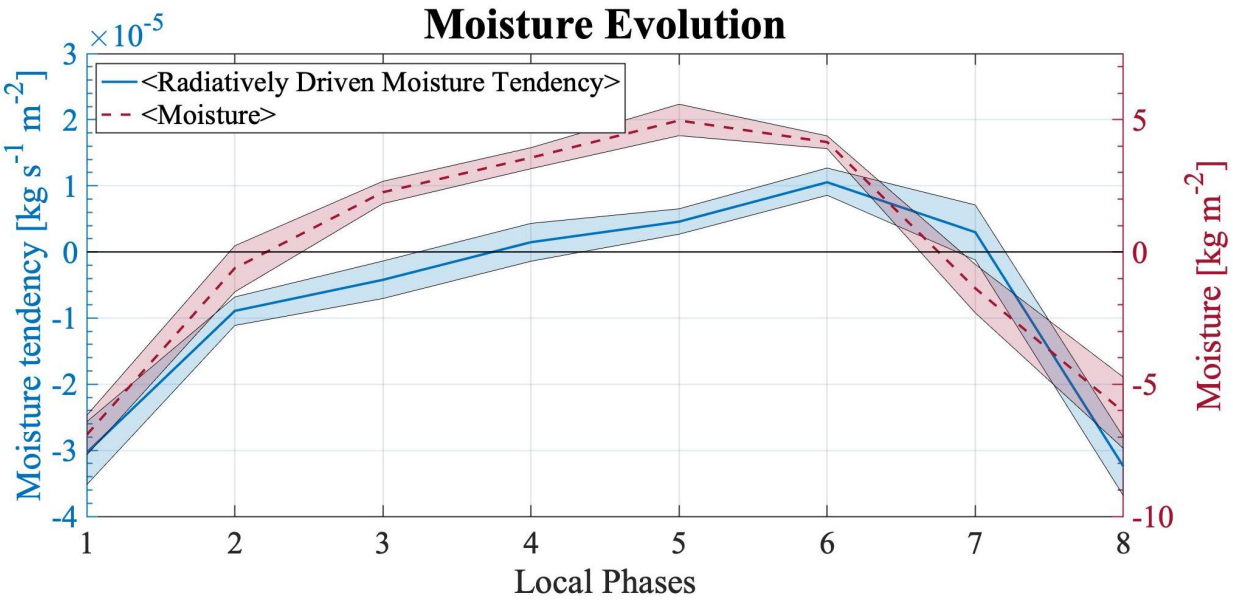

Figure 4.1: Vertically integrated, radiatively-driven moisture tendency, $\langle -\omega_R \partial q/\partial p \rangle'$ (blue, -, left y-axis) and moisture, $\langle q \rangle'$ (red, --, right y-axis) are composited for the MJO, where local phases 1 and 5 represent the suppressed and enhanced phase respectively. Shading represents 95% significance.

Figure 4.2 further elaborates on this point where the same vertically integrated radiatively-driven moisture tendency is shown alongside the actual total moisture tendency, $\langle \partial q/\partial t \rangle'$, in dashed orange. Total moisture tendency maximizes during the transition from the suppressed to enhanced phases to build up moisture ahead of the MJO. As total moisture tendency reaches anomalously negative values in phases 6 and 7, radiatively-driven moisture tendency maximizes and continues to stay positive. The negative contribution from radiatively-driven moisture tendency during phases 1 and 8 are mainly due to the lack of radiative heating through water vapor as Fig. 4.3a shows Q_{clear} to be significantly negative in during these phases. Radiatively-driven moisture tendency contributes to a relatively small amount of negative total moistening during maximum total moisture tendency at phase 2, while a relatively large and positive contribution to total moistening exists during before total moistening minimizes at phases 6 and 7 based on Fig. 4.2. This suggests that radiatively-driven moisture tendency has the largest impact on the moisture field around the enhanced phase compared to the suppressed phase. Furthermore, without this radiatively-driven moistening, the negative total moisture tendency would be larger, suggesting a much more abrupt enhanced to suppressed transition. Therefore, as cloud-radiative feedbacks continue to moisten the MJO, it works against the general pattern of

decreasing moisture suggesting that cloud-radiative interactions prolong/maintain the enhanced phase of the MJO, consistent with what moisture mode theory suggests the cloud-radiative interaction aids in. While this analysis addresses the observed moisture tendency evolution, we will now apply our diagnosed Q_R values from our linear model in chapter 3 to further validate its performance and our results.

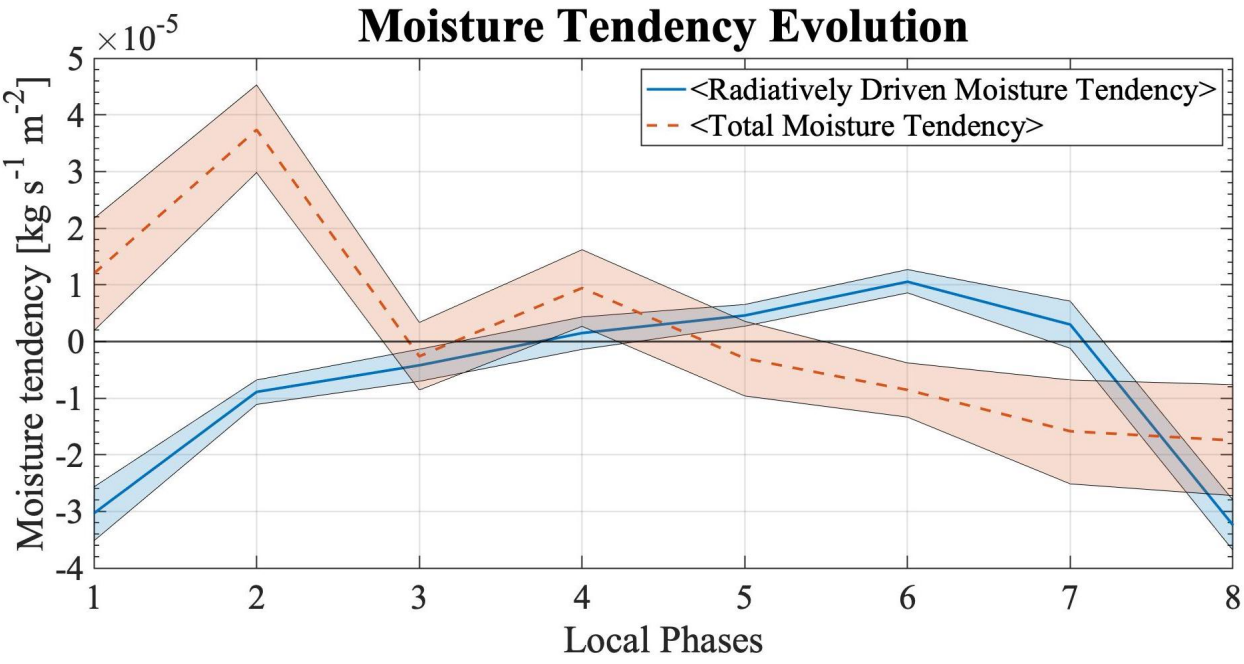

Figure 4.2: Vertically integrated, radiatively-driven moisture tendency, $\langle -\omega_R \partial q/\partial p \rangle'$ (blue, -, left y-axis) and total moisture tendency, $\langle \partial q/\partial t \rangle'$ (orange, --, right y-axis) are composited for the MJO, where local phases 1 and 5 represent the suppressed and enhanced phase respectively. Shading represents 95% significance.

4.3 Diagnosed Cloud-Radiative Moistening

The same analysis will be performed from the previous subsection (section 4.2), however, diagnosed Q_R values from our linear model developed in chapter 3 will be substituted instead of our observed Q_R values, where the linear model diagnoses CRF from cloud type frequency. The use of this linear model allows us to quantify each cloud type's contribution to the radiatively-driven moisture tendency, indicating which cloud types are most influential in the radiatively-driven moistening process. We can first assume that the radiatively-driven moistening is mostly driven by the anomalous radiative heating (Q'_R) as shown in Eq. 9:

$$\langle -Q_R \left(\frac{\partial q/\partial p}{\partial s/\partial p} \right) \rangle' \approx \langle -Q'_R \left(\frac{\partial \bar{q}/\partial p}{\partial \bar{s}/\partial p} \right) \rangle \quad Eq. 9$$

Using the linear model from chapter 3, anomalous radiative heating can be decomposed as the sum of clear-sky radiative heating (Q'_{clear}) and diagnosed cloud-radiative forcing associated with each type of clouds ($\hat{Q}'_{sh}$, $\hat{Q}'_{cg}$, etc.). This allows us to quantify contribution of each cloud type to the net radiatively-driven moistening (Eq. 10)

$$\langle -Q'_R \left(\frac{\partial \bar{q}/\partial p}{\partial \bar{s}/\partial p} \right) \rangle$$

$$\approx \langle -\left(Q'_{clear} + \hat{Q}'_{sh} + \hat{Q}'_{cg} + \hat{Q}'_{dp} + \hat{Q}'_{md} + \hat{Q}'_{av} + \hat{Q}'_{ci} \right) \left(\frac{\partial \bar{q}/\partial p}{\partial \bar{s}/\partial p} \right) \rangle \quad Eq. 10$$

Figure 4.3a again shows the observed vertically integrated radiative moisture tendency evolution in the solid blue line alongside the diagnosed vertically integrated all cloud type radiative moisture tendency in the black dashed line (right hand side of Eq. 10). The diagnosed radiatively-driven moisture tendency follows the observed evolution quite well, both maximizing at phase 6. This suggests that cloud type frequency can suitably diagnose the radiatively-driven moisture tendency, assuring us that the individual cloud type contributions to the radiatively-driven moisture tendency is valid to first order.

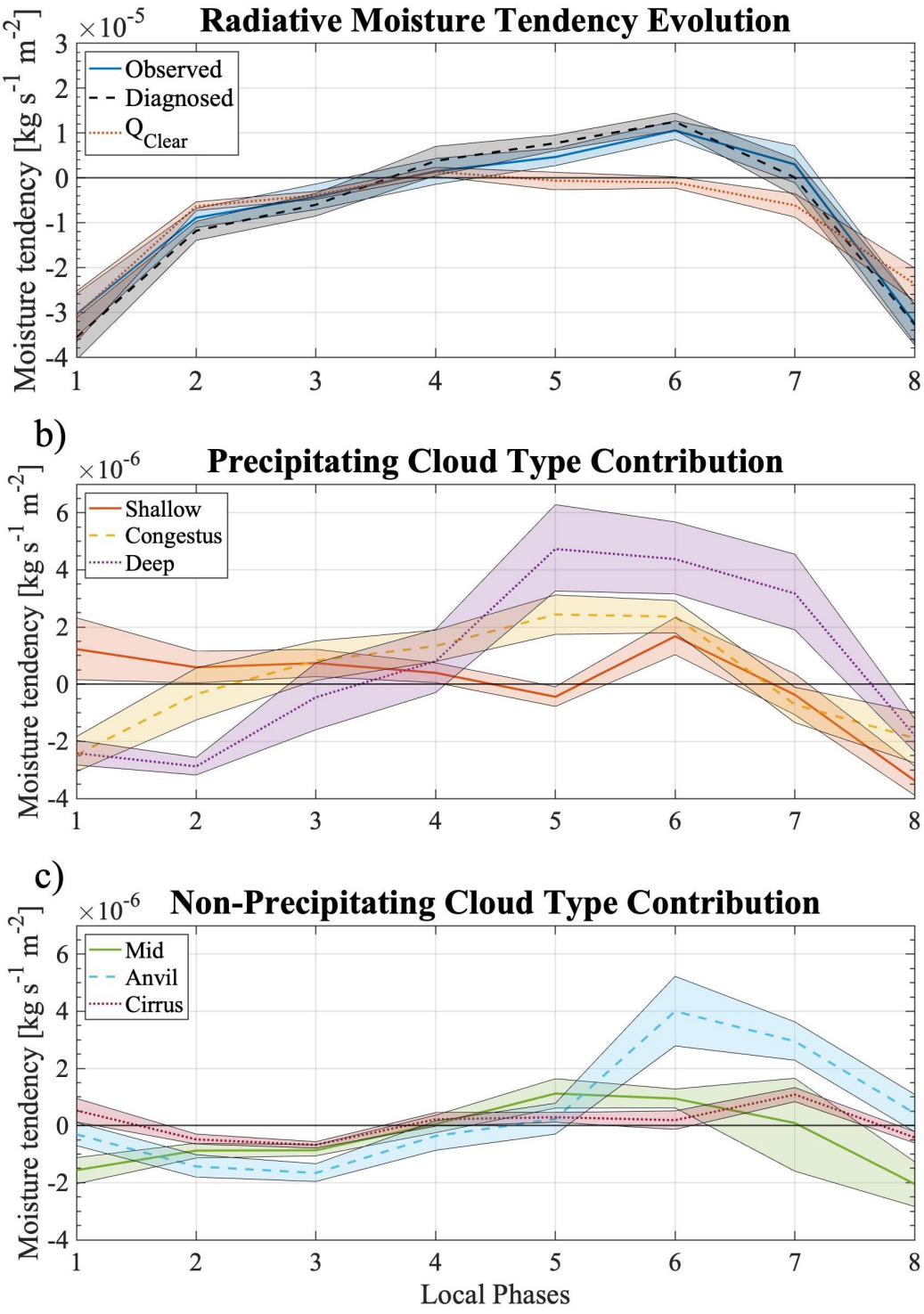

Figure 4.3: a) Vertically integrated, observed radiatively-driven moisture tendency, $\langle -\omega_R \partial q/\partial p \rangle'$ (blue, -), diagnosed (black, --) and the clear-sky radiative contribution (red, ···) are composited for the MJO. Precipitating cloud type (b) and non-precipitating cloud type (c) components of the diagnosed radiative moisture tendency evolution is plotted. Shading represents 95% significance.

Figures 4.3b–c break down the diagnosed evolution seen in the black dashed line in Fig. 4.3a into their respective precipitating and non-precipitating cloud type contributions. Cloud type contribution during the suppressed phase is low other than shallow and cirrus cloud type contributions indicating that most of the contribution is from Q'_{clear}. As the transition to the enhanced phase occurs, all 6-cloud type contribution to radiatively-driven moistening increases. Shallow cloud contribution maximizes during phases 1 and 6, while both congestus and deep cloud types maximize at phase 5 and maintain their amplitude into phase 6 (Fig. 4.3b). The feature of radiatively-driven moistening maximizing or being maintained after the enhanced phase into phase 6 for convective cloud types is a major contributor to the maximizing of radiatively-driven moisture tendency after the enhanced phase has passed. This is somewhat also witnessed with non-precipitating cloud types, specifically anvil cloud types that contribute a significant amount to moistening at phase 6 and staying positive into phase 7, along with cirrus cloud contribution maximizing at phase 7 (Fig. 4.3c). While we show precipitating cloud types altogether contribute more than non-precipitating cloud types in radiatively-driven moistening, note that precipitation is a moisture sink in Eq. 7, something the non-precipitating cloud types do not have. Therefore, although non-precipitating cloud types have a smaller contribution of radiatively-driven moistening than precipitating cloud types, the net contribution to moistening could be higher for non-precipitating cloud types when moisture sink through precipitation is considered. Collectively, we suggest that not one or two cloud types are responsible for the radiatively-driven moistening evolution, but rather the combination of all cloud types maximizing/maintaining their positive moisture tendency leads to the maximizing of radiatively-driven moistening after the enhanced phase. More so, this lagged relationship of radiatively-driven moistening maximizing after the enhanced phase of the MJO has implications on the moisture mode/MJO characteristics, acting to prolong/maintain the enhanced phase.

Chapter 5: Summary and Conclusions

Previous studies have proved theoretically and with observational results that cloud-radiative effects are stronger with low wavenumber waves modes such as the MJO (Adames and Kim, 2016, Inoue et al., 2020, Sakaeda et al., 2020). It has been suggested that the cloud-radiative effects are important to consider in predictive models as it has effects on wave mode characteristics such as propagation, amplitude, and its destabilization mechanism (Lin et al., 2007, Kim et al., 2015, Bony and Emanuel, 2005, Benedict et al., 2020). Cloud-radiative effects are also a key component in some theories attempting to explain the MJO dynamics like moisture mode theory (Yu and Neelin, 1994, Raymond, 2001). This theory suggests that the fundamental dynamics of a moisture mode like the MJO are determined by the processes that control the moisture field. The weak-temperature gradient approximation is assumed under this theory, meaning diabatic heating/cooling is balanced by adiabatic cooling/heating, therefore, cloud-radiative heating can result in vertical motions that advect moisture upwards and moistens the column (Chikira, 2014; Harrop and Hartmann, 2016). Depending on when this moistening maximizes within the wave mode is important as it has implications on wave mode characteristics. More so, determining which cloud types are most contributing to the moistening is important as previous studies have suggested the further spreading of high-clouds to be responsible for the enhanced cloud-radiative effects that are exhibited for low wavenumber wave modes (Lin and Mapes, 2004, Adames and Kim, 2016). The impact of specific cloud types in the MJO moisture budget through their radiative feedback is unknown from an observational standpoint, which is a key gap that this study addresses.

To begin, we utilized data over Addu City, Maldives on Gan Island (0.63S, 73.10E) during the DYNAMO/AMIE field campaign as it provided a diverse set of measurements with multiple MJO, Kelvin, and Westward Inertio Gravity (WIG) events occurring during the campaign. Utilizing filtered precipitation rates for the aforementioned wave modes over Gan Island, provided by the Tropical Rainfall Measuring Mission (TRMM), we produced a local phase definition that tracks wave mode evolution relative to precipitation rates and change in precipitation rates. This allowed for the foundation of an objective intercomparison of measured variables between wave modes, where phase 1 (suppressed) and 5 (enhanced) indicated the times of minimum and maximum local precipitation respectively for each wave mode.

The Pacific Northwest National Laboratory (PNNL) Combined Remote Sensor retrieval algorithm (CombRet) provided cloud base and top heights over Gan Island. After assigning cloud types (i.e., shallow, congestus, deep, mid, anvil, cirrus) to the distribution of top and base heights, it provided a time series of cloud type evolution that can be composited for each wave mode to visualize the evolution of cloud types within wave modes. This analysis suggested that the MJO is characterized by a clear pattern of shallow-to-deep-to-stratiform cloud type evolution with a majority of cloud types maximizing in frequency during phase 6 of the MJO, after the enhanced phase has passed. This does not occur for the Kelvin and WIG waves.

The differences in cloud type evolution between wave modes have implications on cloud-radiative forcing (CRF) evolution, and by utilizing Clouds and Earth's Radiant Energy System (CERES) and CombRet atmospheric CRF measurements, it was found that CRF is stronger as well as lagged with respect to peak rainfall for the MJO compared to the Kelvin and WIG waves. Similar results were also found by utilizing vertically resolved CRF measurements from CombRet. Since this lagged relationship exists for both cloud type and CRF, a linear model was devised to diagnose this relationship further. Linear regressions were constructed for each cloud type where cloud type frequency is used as a diagnostic variable to diagnose CRF. The linear model was able to accurately diagnose column-integrated CRF compared to observational results ($R^2 = 0.78$). Since a linear model was constructed for each cloud type, we were also able to diagnose each cloud type's contribution to CRF. Results showed deep and anvil cloud types to be the largest contributors to CRF within the linear model, suggesting these two cloud types are the most important out of the six to diagnose CRF. Composited diagnosed CRF values also witnessed the lagged CRF evolution that observed measurements saw for the MJO but not for the Kelvin and WIG waves, further validating the cloud type relationship with CRF and the performance of the linear model.

Since the MJO is often described to be a moisture mode, it was important to relate the cloud-radiative heating to quantifying the contribution to total moistening. Interestingly, vertically integrated radiatively-driven moisture tendency maximized after vertically integrated moisture maximized, and continued to contribute positive moistening as moisture decreased, acting against the total moisture tendency. This result suggests that cloud-radiative effects act to prolong/maintain the MJO enhanced phase. Furthermore, applying diagnosed CRF measurements from the linear model to diagnose radiatively-driven moisture tendency per cloud

type followed observed results, further validating the model's performance. Cloud type contribution to the diagnosed radiative moistening showed that the combination of cloud types maximizing and maintaining their contribution after the enhanced phase resulted in the radiatively-driven moisture tendency lag rather than just because of high-clouds or deep and anvil clouds.

To summarize, this observational study found that the MJO exhibits a clear pattern of cloud type evolution, where clouds begin shallow early on and deepen and stratiform during the transition to enhanced, unlike the Kelvin and WIG waves. Also, only the MJO witnesses most cloud types maximizing in frequency after the enhanced phase of the MJO. It was also shown that the MJO CRF is larger and lags precipitation compared to the Kelvin and WIG waves. This relationship was tested through a linear model and was shown to replicate observed CRF evolutions by simply knowing cloud type frequencies. The added diabatic heating through radiative processes translates to moistening under WTG approximation. The radiatively-driven moisture tendency maximized after the enhanced phase when total moisture tendency was negative, and continued to stay positive, suggesting cloud-radiative effects contribute to the prolonging/maintaining of the enhanced phase of the MJO. After quantifying each cloud types contribution to the radiatively-driven moistening, it was shown that the combination of cloud types is responsible for the maximizing of observed and diagnosed radiative driven moistening after the enhanced phase, not solely because of high clouds or deep and anvil clouds.

We would like to quantify all terms in the moisture tendency equation (Eq. 7) for future work to get a complete understanding on how moistening through cloud-radiative effects compares with the other terms. It would also be worthwhile to analyze data sets on a larger temporal and spatial scale to examine this relationship outside of the local region of Gan Island and to add more significance since it was difficult to achieve throughout this study.

This study is one of the first to exist that we know of that compares observed CRF evolution between various wave modes. The method used allowed us to pursue the relationship between cloud-radiative effects and wavenumber, which provided observational results that support theoretical and observational claims that were made about the decreasing cloud-radiative feedback parameter with increasing wavenumber relationship. A slightly different approach on why this relationship exists was suggested however, stating that a combination of cloud types is responsible for the relationship existing, not just high clouds or deep and anvil clouds, furthering

our understanding of why this unique relationship exists. This study also provided observational analysis on how radiatively-driven moistening can act to prolong/maintain the enhanced phase of the MJO under moisture mode theory, reinforcing previous modeling-based studies that have witnessed similar results. All of this furthers our understanding of the MJOs dynamics, putting more emphasis on the importance of understanding cloud-radiative effects within the MJO.

Reference List

Adames, Á. F., & Kim, D. (2016). The MJO as a dispersive, convectively coupled moisture wave: Theory and observations. *Journal of the Atmospheric Sciences*, *73*(3), 913–941. https://doi.org/10.1175/JAS-D-15-0170.1

Alvarez, M. S., Vera, C. S., Kiladis, G. N., & Liebmann, B. (2016). Influence of the Madden Julian Oscillation on precipitation and surface air temperature in South America. *Climate Dynamics*, *46*(1–2), 245–262. https://doi.org/10.1007/s00382-015-2581-6

Benedict, J. J., Medeiros, B., Clement, A. C., & Olson, J. G. (2020). Investigating the Role of Cloud-Radiation Interactions in Subseasonal Tropical Disturbances. *Geophysical Research Letters*, *47*(9), 1–11. https://doi.org/10.1029/2019GL086817

Benedict, J. J., & Randall, D. A. (2007). Observed characteristics of the MJO relative to maximum rainfall. *Journal of the Atmospheric Sciences*, *64*(7), 2332–2354. https://doi.org/10.1175/JAS3968.1

Bony, S., & Emanuel, K. A. (2005). On the role of moist processes in tropical intraseasonal variability: Cloud-radiation and moisture-convection feedbacks. *Journal of the Atmospheric Sciences*, *62*(8), 2770–2789. https://doi.org/10.1175/JAS3506.1

Chikira, M., 2014: Eastward-propagating intraseasonal oscillation represented by Chikira–Sugiyama cumulus parameterization. Part II: Understanding moisture variation under weak temperature gradient balance. J. Atmos. Sci., 71, 615–639, doi:10.1175/JAS-D-13-038.1.

Ciesielski, P. E., Johnson, R. H., Jiang, X., Zhang, Y., & Xie, S. (2017). Relationships between radiation, clouds, and convection during DYNAMO. *Journal of Geophysical Research*, *122*(5), 2529–2548. https://doi.org/10.1002/2016JD025965

Feng, Z., McFarlane, S. A., Schumacher, C., Ellis, S., Comstock, J., & Bharadwaj, N. (2014). Constructing a merged cloud-precipitation radar dataset for tropical convective clouds during the DYNAMO/AMIE experiment at Addu Atoll. *Journal of Atmospheric and Oceanic Technology*, *31*(5), 1021–1042. https://doi.org/10.1175/JTECH-D-13-00132.1

Genio, A., & Chen, Y. (2015). Journal of Geophysical Research : Atmospheres oscillation as seen by the A-Train. *Journal of Geophysical Research Atmospheres*, 5344–5356. https://doi.org/10.1002/2015JD

Harrop, B., & Hartmann, D. (2016). The role of cloud radiative heating within the atmosphere on the high cloud amount and top-of-atmosphere cloud radiative effect. *Journal of Advances in Modeling Earth Systems*, *8*, 1358–1375. https://doi.org/10.1002/2016MS000625

Hendon, H. H., Wheeler, M., & Zhang Chidong. (2007). Seasonal Dependence of the MJO – ENSO Relationship. *Journal of Climate*, *20*(Lau 2005), 531–543. https://doi.org/https://doi.org/10.1175/JCLI4003.1

Huffman, G. J., Adler, R. F., Bolvin, D. T., Gu, G., Nelkin, E. J., Bowman, K. P., Hong, Y., Stocker, E. F., & Wolff, D. B. (2007). The TRMM Multisatellite Precipitation Analysis (TMPA): Quasi-global, multiyear, combined-sensor precipitation estimates at fine scales. *Journal of Hydrometeorology*, *8*(1), 38–55. https://doi.org/10.1175/JHM560.1

Inoue, K., Adames, Á. F., & Yasunaga, K. (2020). Vertical velocity profiles in convectively coupled equatorial waves and MJO: New diagnoses of vertical velocity profiles in the wavenumber-frequency domain. *Journal of the Atmospheric Sciences*, *77*(6), 2139–2162. https://doi.org/10.1175/JAS-D-19-0209.1

Jiang, X., Adames, Á. F., Kim, D., Maloney, E. D., Lin, H., Kim, H., Zhang, C., DeMott, C. A., & Klingaman, N. P. (2020). Fifty Years of Research on the Madden-Julian Oscillation: Recent Progress, Challenges, and Perspectives. *Journal of Geophysical Research: Atmospheres*, *125*(17), 1–64. https://doi.org/10.1029/2019JD030911

Kiladis, G. N., Straub, K. H., & Haertel, P. T. (2005). Zonal and vertical structure of the Madden-Julian oscillation. *Journal of the Atmospheric Sciences*, *62*(8), 2790–2809. https://doi.org/10.1175/JAS3520.1

Kim, D., Ahn, M. S., Kang, I. S., & Del Genio, A. D. (2015). Role of longwave cloud-radiation feedback in the simulation of the Madden-Julian oscillation. *Journal of Climate*, *28*(17), 6979–6994. https://doi.org/10.1175/JCLI-D-14-00767.1

Klingaman, N. P., Woolnough, S. J., Jiang, X., Waliser, D., Xavier, P. K., Petch, J., Caian, M., Hannay, C., Kim, D., Ma, H. Y., Merryfield, W. J., Miyakawa, T., Pritchard, M., Ridout, J. A., Roehrig, R., Shindo, E., Vitart, F., Wang, H., Cavanaugh, N. R., … Zhang, G. J. (2015). Vertical structure and physical processes of the Madden-Julian oscillation: Exploring key model physics in climate simulations. *Journal of Geophysical Research*, *120*(10), 4690–4717. https://doi.org/10.1002/2014JD022375

Liebmann, B., Hendon, H., & Glick, D. (1994). The Relationship Between Tropical Cyclones of the Western Pacific and Indian Oceans and the Madden-Julian Oscillation. *Journal of the Meteorological Society of Japan*, *72*, 401–411. https://doi.org/https://doi.org/10.2151/jmsj1965.72.3_401

Lim, Y., Son, S. W., & Kim, D. (2018). MJO prediction skill of the subseasonal-to-seasonal prediction models. *Journal of Climate*, *31*(10), 4075–4094. https://doi.org/10.1175/JCLI-D-17-0545.1

Lin, J. L., Kim, D., Lee, M. I., & Kang, I. S. (2007). Effects of cloud-radiative heating on atmospheric general circulation model (AGCM) simulations of convectively coupled equatorial waves. *Journal of Geophysical Research Atmospheres*, *112*(24), 1–19. https://doi.org/10.1029/2006JD008291

Lin, J., Mapes, B., Zhang, M., & Newman, M. (2004). Stratiform precipitation, vertical heating profiles, and the Madden-Julian oscillation. *Journal of the Atmospheric Sciences*, *61*(3), 296–309. https://doi.org/10.1175/1520-0469(2004)061<0296:SPVHPA>2.0.CO;2

Madden, R. A., & Julian, P. R. (1971). Detection of a 40–50 Day Oscillation in the Zonal Wind in the Tropical Pacific. *Journal of the Atmospheric Sciences*, *28*(5). https://doi.org/10.1175/1520-0469(1971)028<0702:doadoi>2.0.co;2

Maloney, E. D., 2009: The moist static energy budget of a composite tropical intraseasonal oscillation in a climate model. J. Climate, 22, 711–729.

Martin, E. R., & Schumacher, C. (2011). Modulation of Caribbean precipitation by the Madden-Julian oscillation. *Journal of Climate*, *24*(3), 813–824. https://doi.org/10.1175/2010JCLI3773.1

Mapes, B. E. (1993). Gregarious Tropical Convection. *Journal of the Atmospheric Sciences*, *50*(13), 2026–2037. https://doi.org/10.1175/1520-0469(1993)050<2026:GTC>2.0.CO;2

Neelin, J. D., & Yu, J.-Y. (1994). Modes of Tropical Variability under Convective Adjustment and the Madden-Julian Oscillation. Part I: Analytical Theory. *Journal of the Atmospheric Sciences*, *51*(13). https://doi.org/https://doi.org/10.1175/1520-0469(1994)051<1876:MOTVUC>2.0.CO;2

Powell, S. W., & Houze, R. A. (2013). The cloud population and onset of the Madden-Julian Oscillation over the Indian Ocean during DYNAMO-AMIE. *Journal of Geophysical Research Atmospheres*, *118*(21), 11,979-11,995. https://doi.org/10.1002/2013JD020421

Powell, S. W., Houze, R. A., & Brodzik, S. R. (2016). Rainfall-type categorization of radar echoes using polar coordinate reflectivity data. *Journal of Atmospheric and Oceanic Technology*, *33*(3), 523–538. https://doi.org/10.1175/JTECH-D-15-0135.1

Raymond, D. J. (2001). A New Model of the Madden–Julian Oscillation DAVID. *Journal of the Atmospheric Sciences*, *58*, 2807–2819.

Riley, E. M., & Mapes, B. E. (2009). Unexpected peak near -15°C in CloudSat echo top climatology. *Geophysical Research Letters*, *36*(9), 1–5. https://doi.org/10.1029/2009GL037558

Riley, E. M., Mapes, B. E., & Tulich, S. N. (2011). Clouds associated with the Madden-Julian oscillation: A new perspective from Cloudsat. *Journal of the Atmospheric Sciences*, *68*(12), 3032–3051. https://doi.org/10.1175/JAS-D-11-030.1

Sakaeda, N., Dias, J., & Kiladis, G. N. (2020). The Unique Characteristics and Potential Mechanisms of the MJO-QBO Relationship. *Journal of Geophysical Research: Atmospheres*, *125*(17), 1–22. https://doi.org/10.1029/2020JD033196

Steiner, M., Houze Jr., R. A., & Yuter, S. (1995). Climatological Characterization of Three-Dimensional Storm Structure from Operational Radar and Rain Gauge Data. *Journal of Applied Meteorology*, *34*, 1978–2007. https://doi.org/https://doi.org/10.1175/1520-0450(1995)034%3C1978:CCOTDS%3E2.0.CO;2

Wheeler, M. C., & Hendon, H. H. (2004). An all-season real-time multivariate MJO index: Development of an index for monitoring and prediction. *Monthly Weather Review*, *132*(8), 1917–1932. https://doi.org/10.1175/1520-0493(2004)132<1917:AARMMI>2.0.CO;2

Wheeler, M., & Kiladis, G. N. (1999). Convectively Coupled Equatorial Waves: Analysis of Clouds and Temperature in the Wavenumber-Frequency Domain. *Journal of the Atmospheric Sciences*, *56*(3), 374–399. https://doi.org/10.1175/1520-0469(1999)056<0374:CCEWAO>2.0.CO;2

Wielicki, B. A., Barkstrom, B. R., Harrison, E. F., Lee, R. B., Smith, G. L., & Cooper, J. E. (1996). Clouds and the Earth's Radiant Energy System (CERES): An Earth Observing System Experiment. *Bulletin of the American Meteorological Society*, *77*(5), 853–868. https://doi.org/10.1175/1520-0477(1996)077<0853:CATERE>2.0.CO;2

Wolding, B., Maloney, E. D., & Branson, M. (2016). Vertically resolved weak temperature gradient analysis of the Madden-Julian Oscillation in SP-CESM. *Journal of Advances in Modeling Earth Systems*, *8*(4), 1586–1619. https://doi.org/10.1002/2016MS000724

Yanai, M., Esbensen, S., & Chu, J.-H. (1973). Determination of Bulk Properties of Tropical Cloud Clusters from Large-Scale Heat and Moisture Budgets. *Journal of the Atmospheric Sciences*, *30*(4), 611–627. https://doi.org/https://doi.org/10.1175/1520-0469(1973)030%3C0611:DOBPOT%3E2.0.CO;2

Yasunari, T. (1979). Cloudiness Fluctuations Associated with the Northern Hemisphere Summer Monsoon. *Journal of the Meteorological Society of Japan. Ser. II*, *57*(3), 227–242. https://doi.org/10.2151/jmsj1965.57.3_227

Zhu, H., & Hendon, H. H. (2015). Role of large-scale moisture advection for simulation of the MJO with increased entrainment. *Quarterly Journal of the Royal Meteorological Society*, *141*(691), 2127–2136. https://doi.org/10.1002/qj.2510